International Journal of Biological Macromolecules 327 (2025) 147216

Contents lists available at ScienceDirect

International Journal of Biological Macromolecules

journal homepage: www.elsevier.com/locate/ijbiomac

Asymmetric T-segment binding and gate dynamics govern the final stages of the type IIA topoisomerase catalytic cycle

Kristina Stevanović [a,b], Barbara Herlah [a], Matic Pavlin [c], Andrej Perdih [a,d,*]

[a] Theory Department, National Institute of Chemistry, Hajdrihova 19, 1000 Ljubljana, Slovenia
[b] Laboratory of Bioinformatics and Computational Chemistry, Institute of Nuclear Sciences Vinca, Serbia
[c] Department of Catalysis and Chemical Reaction Engineering, National Institute of Chemistry, Hajdrihova 19, 1000 Ljubljana, Slovenia
[d] University of Ljubljana, Faculty of Pharmacy, Aškerčeva 7, 1000 Ljubljana, Slovenia

ARTICLE INFO

Keywords:
Type IIA DNA topoisomerase
T-segment
C-gate
Catalytic cycle
Molecular dynamics

ABSTRACT

Type IIA DNA topoisomerases are molecular nanomachines that alter DNA topology during essential cellular processes. The final steps of their catalytic cycle, after translocation of the transported (T-) segment into the C-gate, are still not fully understood. Here, we performed all-atom molecular dynamics simulations of several conformational states of *Saccharomyces cerevisiae* topoisomerase IIA, each with a T-segment inserted into the C-gate. Bound ATP and ADP nucleotides allosterically modulated the N-gate dynamics, likely stabilizing the dimer and preventing premature dissociation. The T-segment was asymmetrically bound and stabilized within the C-gate by positively charged residues, and this gate remained structurally rigid, highlighting its role as a retention site. The positioning of the T-segment in the C-gate allosterically influenced the G-segment to a straighter geometry that favors religation and release. Our simulations support coordinated release of DNA segments and point to a potentially important role for dynamic communication between the gates in the mechanism. These results provide new insights into the late stages of the catalytic cycle and highlight the intertwined roles of nucleotide binding, DNA topology and coupled protein domain dynamics in regulating this important enzyme.

1. Introduction

DNA topoisomerases (topo) control and regulate the topological state of DNA in all eukaryotic and prokaryotic cells and are even present in some viruses [1,2]. They are classified into type I and type II subfamilies, with the latter further subdivided into topo IIA and topo IIB subfamilies [3]. The first members of type IIA topoisomerases were discovered around 45 years ago, and they play a crucial role in DNA replication, transcription, and chromosome segregation [3,4].

Due to their critical involvement in normal cell function, inhibition of type IIA topoisomerases is the underlying mechanism of many drugs used either as anticancer or antibacterial agents [5]. For example, topoisomerase II poisons such as etoposide and doxorubicin, which stabilize the transient covalent complex between topo IIA and DNA, are commonly used in chemotherapy. As these agents can cause harmful side effects such as secondary malignancies and cardiotoxicity [6,7], consequently either selective topo II poisons [8] or mechanistically diverse catalytic inhibitors [9–12] are currently being developed to mitigate their side effects.

The understanding of the topo IIA mechanism of action at the molecular level remains the focus of intensive research [13]. In solution topo IIA exists as stable homodimer [14] and the molecular motor forms three distinct topological and functional segments: N-gate, DNA-gate, and C-gate (Fig. 1A). Structural studies of type IIA topoisomerases have primarily focused on an isolated DNA binding/cleavage core (DNA-gate and C-gate) [15,16] while the ATPase domain comprising the N-gate has generally been studied separately with the ATP-dependent rigid body movement of structural modules being observed [17,18].

An important milestone in topo IIA research was the determination of the crystal structure of fully catalytic homodimer of *Saccharomyces cerevisiae* topoisomerase IIA, which provided a detailed structural description, including all three functional gates (Fig. 1A) [19]. The N-gate, where the Transport (T-) segment of DNA binds, is formed by two ATPase domains, each comprising a GHKL and a transducer domain [20]. The DNA-gate, responsible for binding and cleaving the Gate (G-) segment of the DNA, consists of the TOPRIM (TOpoisomerase-PRIMmase), Winged-Helix Fomain (WHD), and tower domains [21]. Within the WHD, a catalytic tyrosine (Tyr782) residue is located, which,

* Corresponding author at: National Institute of Chemistry, Hajdrihova 19, SI-1001 Ljubljana, Slovenia.
E-mail address: andrej.perdih@ki.si (A. Perdih).

https://doi.org/10.1016/j.ijbiomac.2025.147216
Received 8 July 2025; Received in revised form 22 August 2025; Accepted 28 August 2025
Available online 29 August 2025

assisted by two Mg^{2+} ions at each cleavage site, cleaves the G-segment of the DNA, presumably via a two-metal mechanism [22].

Beyond the DNA-gate, the enzyme extends into the coiled-coil regions composed of α-helices, which form the C-gate. This region captures the T-segment after it passes through the DNA-gate and subsequently releases it from the enzyme. The most structurally ambiguous region remains the C-terminal domain (CTD), which is believed to be largely intrinsically disordered, as 3D structural data are still lacking. The CTD has been proposed to play multiple roles: it may be involved in the DNA recognition process, acts as a scaffold to recruit mitotic regulators to the centromeres, and regulates the catalytic cycle [23,24].

Recent cryo-EM studies of the human topoisomerase IIα have elucidated the movement of the N-gate, as well as dynamics within the DNA-gate, and revealed the presence of α-helices connecting the N-terminal domain to the DNA-binding/cleavage core [25]. The conformational landscape of type II topoisomerases has been further advanced through crystal and cryo-EM structures of the type II topoisomerase from the African swine fever virus, offering new insights into structure-function relationship including the T-segment binding within the C-gate [26–28]. A further level of complexity arises since CTD as well as catalytic domains of the homodimer can undergo post-translational modifications, such as phosphorylation and acetylation, which also regulate the activity of the topoisomerase IIA [29,30]. The function of topoisomerase IIA is also modulated by its interaction with chromatin, adding another layer of complexity to its regulation [31].

The combination of structural and biochemical data culminated in the current model on type IIA topoisomerases mode of action, known as the "two-gate model" of the catalytic cycle (Fig. 1B) [32]. In this model, topoisomerase IIA (*Structure 1*) first binds the G-segment in the DNA-gate (*Structure 2*) and the T-segment at the ATP gate. Two ATP molecules then bind to the ATPase domain of the N-gate, which leads to the dimerization of the N-gate and entrapment of the T-segment (*Structure 3*) [33]. Two catalytic tyrosine residues cleave the G-segment in the presence of Mg^{2+} ions [22,34], creating a covalent 5′-phosphotyrosine-DNA intermediate (*Structure 4*). This cleavage creates a transient break, allowing the T-segment to pass through the break, accompanied by the hydrolysis of one ATP molecule to ADP (*Structure 5*) [15,35]. The role of ATP hydrolysis is not yet fully understood, as the process of topology simplification requires a relatively low energy input [36]. One possibility is that it facilitates the conformational change required for the T-segment passage to the C-gate. Another option suggested was that ATP hydrolysis plays an allosteric role by modulating the separation of protein–protein interfaces in the dimer, which helps to prevent random double-strand DNA breaks (DSBs), a potentially destructive event for the cell [37–39]. After T-segment transport is complete, the cleaved G-segment is religated, and the second ATP molecule is hydrolyzed to ADP (*Structure 6)*. The function of this second ATP hydrolysis is still ambiguous, but it is thought to facilitate communication between the ATPase and the DNA cleavage/ligation domains, helping reset the enzyme for the next cycle [40]. Finally, as the ADP molecules dissociate, both the C-gate and the N-gate open, releasing the T-segment and the G-segment (*Structure 7*), thereby resetting the molecular motor to be ready for another catalytic cycle.

In our effort to better understand the catalytic cycle of type IIA topoisomerases, we performed all-atom molecular dynamics simulations of the full-length yeast enzyme in various conformations. Our analysis focused primarily on states preceding the passage of the T-segment through the cleaved G-segment; in some of these configurations the T-segment was positioned within the N-gate (Fig. 1B). The rotational movement of the ATPase dimer and sliding of the DNA-gate appeared to be intrinsic properties of the enzyme that may facilitate the T-segment transport. Furthermore, presence of ATP stabilized the T-segment within the N-gate, suggesting its role in optimally positioning the G-segment and preventing unwanted double-strand breaks during catalysis [41,42].

Having computationally explored several configurations in the first part of the catalytic cycle, in this study we turned our attention to the conformational landscape of type IIA topoisomerase after passage of the T-segment through the cleaved G-segment. Based on the proposed catalytic cycle, we constructed four configurations by incorporating the T-segment into the C-gate, varying the presence of ATP/ADP molecules in their binding sites, and altering the state of the G-segment. All-atom simulations provided insights in the effects of DNA and ATP

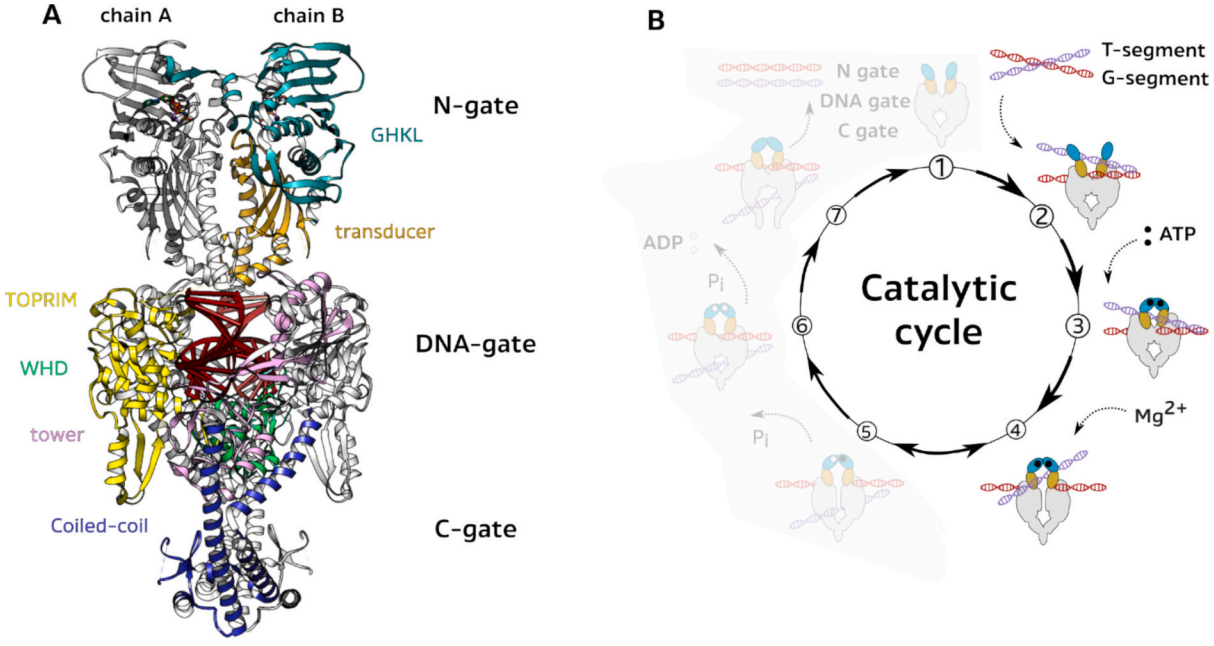

Fig. 1. (**A**) Crystal structure of *Saccharomyces cerevisiae* type IIA topoisomerase with bound DNA in the DNA-gate (PDB: 4GFH), marking the positions of the N-, DNA-, and C-gates. Domain annotations include the GHKL (residues 6-256), transducer (257-416), TOPRIM (417-698), WHD (699-796), tower (797-989), and coiled-coil (990-1171) regions. The domain boundaries are approximate. (**B**) The catalytic cycle of the type IIA topoisomerases, with a focus on the steps before T-segment transport, which have already been explored through molecular simulations.

hydrolysis on local and global protein dynamics and served as a comparison with previous simulations as well as with available experimental data. In this way, we uncover previously hidden details of the molecular choreography that orchestrates the actions of type IIA topoisomerases in part of the catalytic cycle when the T-segment is present in the C-gate.

2. Results

2.1. Constructing type IIA topoisomerase configurations with T-segment in the C-gate

Molecular dynamics simulations were performed with a fully catalytic homodimer of yeast topo IIA, which has already provided valuable insights into the behavior of the enzyme prior to passage of the T-segment. This study focuses on investigating the dynamics of conformations occurring in the second part of the catalytic cycle, i.e. after the T-segment has already been transported. In the catalytic cycle this would correspond to *S-7* (Fig. 2). In the crystal structure (PDB: 4GFH) the available space in the C-gate is wide enough to easily accommodate and bind the T-segment. To generate these conformations, we used two configurations derived from X-ray structure 4GFH from our previous studies: one a direct analogue (previously referred as "**cleaved"**, Fig. 2 A) [41] and the second conformation with the T-segment inserted into the N-gate and the G-segment religated; (referred to as **2Pre** Fig. 2B) [42].

The "**cleaved"** structure was used as a starting point to create configurations resembling *Structures 5* and *6* in the catalytic cycle. The T-segment was structurally identical to the G-segment present in the yeast topo IIA structure. It was first relaxed and then manually placed in the C-gate. Next, **1Bro** and **2Bro** configurations were created by modifying ATP molecules to ADP/ATP (**1Bro**) and ADP/ADP molecules pairs (**2Bro**) by deleting the γ-phosphate in ATP (Fig. 2C-D and Table 1). The abbreviation "**Bro"** was derived from the term that stands for "*broken"* which vividly portrays the cleaved state of the DNA G-segment.

Similarly, starting from **2Pre** structure, the T-segment was removed from the N-gate and by aligning **2Pre** and **1Bro** the T-segment was inserted in the C-gate. Next, both ATPs were either modified to ADP or completely removed from the ATP binding sites to obtain configurations **3Rel** and **4Rel** (Fig. 2E-F and Table 1). The same starting position of the T-segment allowed for a more consistent comparison in all simulations. The abbreviation **"Rel"** stands for "*religated"* to describe the state of the DNA in these configurations. The **2Pre** was chosen as a starting and reference structure as the N-gate is in a more open position compared to the X-ray structure to enable the placement of the T-segment. This allowed further assessment of the N-gate dynamics as well as the allosteric effect of nucleotides bound to the ATP gate, particularly on the opening/closing of the N-gate.

All topo IIA configurations were solvated and equilibrated before undergoing 1 μs-long production runs using classical molecular dynamics (MD) simulations. MD simulations inherently explore the potential energy landscape in a manner that the system can become trapped in a local minimum, thus limiting the exploration of other relevant conformations. To overcome this limitation, we ran two additional independent replicas in the length of 0.5 μs for each of the four configurations. Such approach enhances the conformation sampling and allows the exploration of a larger region of the available potential energy surface [43].

2.2. Global dynamics, allosteric effect of the bound nucleotides and influence of the bound T-segment in the C-gate

The conformational stability was initially investigated by global dynamics, with equilibrium being reached for all systems after about 100 ns of the simulation based on RMSD. The configurations with cleaved G-segment exhibited greater stability than the religated DNA structures with average RMSD values of 3.3 ± 0.3 Å (**1Bro**) and 3.9 ± 0.7 Å (**2Bro**) compared to 5.2 ± 0.5 (**3Rel**) and 4.7 ± 0.4 Å (**4Rel**) (Fig. 3A). These observations are consistent with the differences in the stability of analogous topo IIA structures observed in the configurations prior to T-segment passage [42]. **1Bro** and **2Bro** conformations with cleaved G-segment were comparable, yet RMSD of **2Bro** with only ADP molecules shows a slight increase, possibly indicating some effect of ATP hydrolysis on protein stabilization. The higher RMSD value in **3Rel** compared to **4Rel** can also be attributed to the observed closure of the N-gate that occurred in the first part of trajectory, to a similar position as observed in **1Bro** and **2Bro,** suggesting that the sole presence of ADP molecules may stabilize the N-gate in a more closed position. A similar trend in RMSD values was observed across replicas, with no major deviations observed (Fig. S1). In the manuscript, the results of the longer 1 μs simulations are mainly presented in the Figures, while the data of the replicas are mostly included in the Supplementary material.

Local protein dynamics showed asymmetric behavior between the monomers, which is consistent with behavior for configurations observed prior to T-segment passage (Fig. 3B-I) [42] as well as the assumed mechanism of topo IIA catalytic cycle acting via a sequential ATP hydrolysis [44]. The presence of ATP or ADP appears to influence the dynamics of the N-gate even in the absence of the T-segment in the N-gate. **1Bro** showed the lowest residue dynamics in the ATPase domains, while in **4Rel**, in which both nucleotides were removed from the active site and the DNA was religated, the N-gate residues exhibited the most significant deviations. In **2Bro** structure, in which the remaining ATP was replaced by ADP, the mobility of the upper GHKL domain increased slightly compared to **1Bro**. This trend continued in the **3Rel** structure, in which the G-segment is religated and the ADP/ADP-bound nucleotide pair was still present. The especially strong asymmetric dynamics of the individual ATPase domains can be attributed here to the closing of the N-gate, which occurs predominantly through the movement of one ATPase domain. In general ATP hydrolysis and subsequent ADP dissociation increase N-gate flexibility, a trend observed across all replicas (Figs. S2-S3). Furthermore, the residues at the interface between DNA-, N-, and C-gates showed significant fluctuations, although the pattern of these fluctuations varied across in different configurations.

In contrast to the considerable dynamics observed at the N-gate, where significant flexibility occurred in the absence of the bound T-segment, the C-gate with the inserted T-segment did not show a substantial increase in flexibility compared to previous configurations [42]. The main flexibility was observed in residues where the monomers interact, which likely plays a role in the capture and release of the T-segment, The intensity of this flexibility varied between the replicas.

Another local substantial dynamic feature observed was that of the TOPRIM domain residues 526-608, comprised of an α-helix and three β-sheet substructures. Its dynamics has been consistently observed in topo IIA configurations simulated to date [41,42]. We previously proposed that its intense movement may reflect insufficient interactions between this region and the unresolved C-terminal domain (CTD), which is believed to be disordered and whose function is regulated by phosphorylation at multiple residues. Simulations of the new configurations with the T-segment bound in the C-gate provide new perspectives by revealing favorable interactions between the T-segment and TOPRIM, suggesting this domain is involved via this component in the stabilization and proper capture of the T-segment after T-segment transport.

2.3. Energetic hotspots and asymmetric binding define T- and G-segment interactions in the topo IIA gates

The geometric features of topo IIA configurations were corroborated by end-point MM/GBSA free energy calculations, which revealed a consistent pattern of three engaged hotspot regions within the protein. These include residues in the upper part of the N-gate (e.g. Tyr12), residues near the DNA-gate (e.g. Phe343 and Arg507) and residues at the end of the C-gate (e.g. Arg1120, Ile1121, Trp1122, and Leu1124)

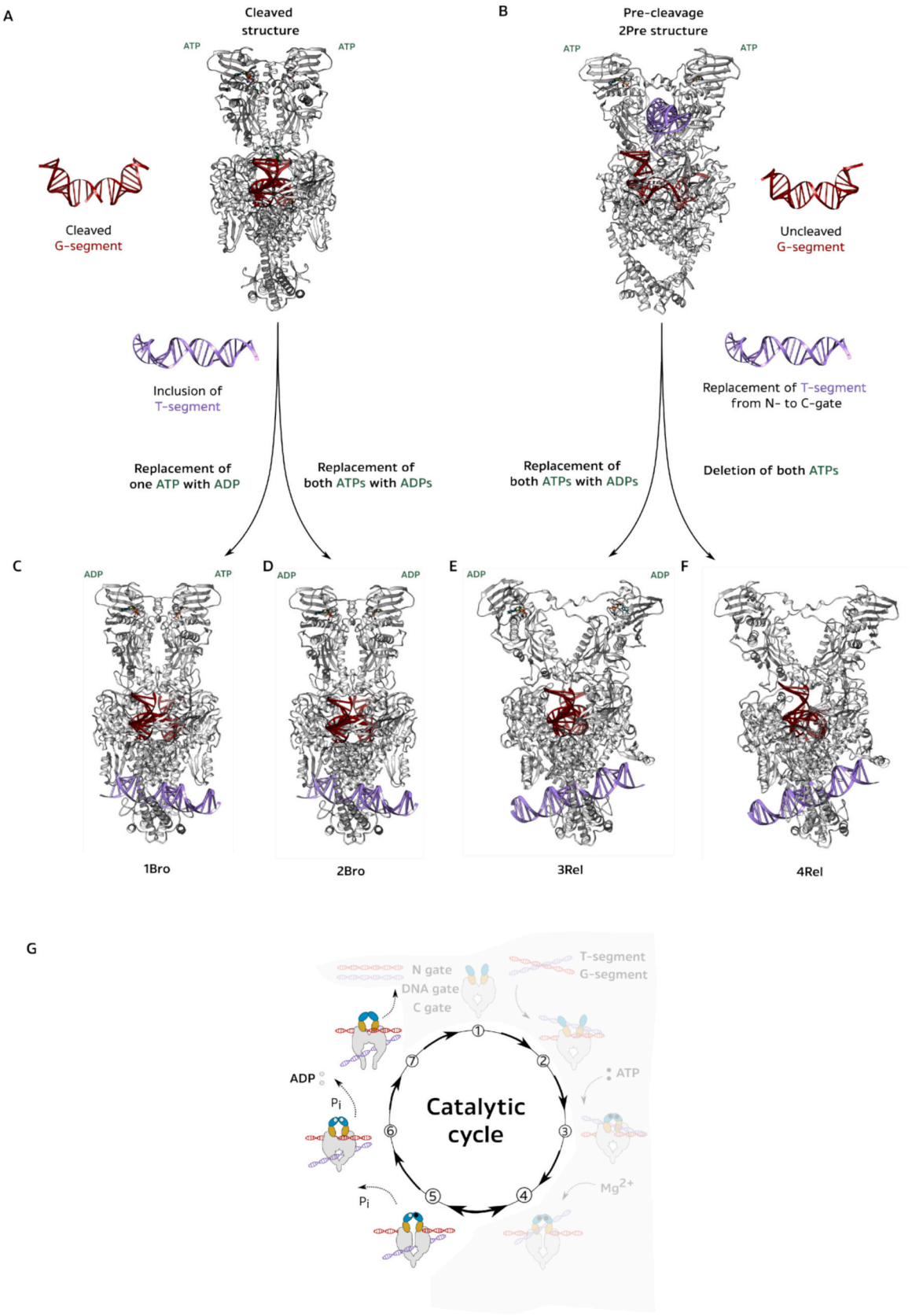

Fig. 2. (**A-B**) Available configurations of topo IIA used as starting points; (**C-F**) Construction process to topo IIA configurations **1Bro**, **2Bro**, **3Rel** and **4Rel** simulated in this study; (**G**) Schematic representation of the approximate part of the topo IIA catalytic cycle modeled by a new set of topo IIA configurations.

Table 1
Topo IIA configurations, their main structural distinctions and approximate positions in the catalytic cycle.

Structure	G-segment DNA-gate	T-segment C-gate	ATP/ADP (ATP binding site)	Catalytic topo II cycle location
1Bro	Cleaved	Inserted	ATP and ADP	~5
2Bro	Cleaved	Inserted	ADP and ADP	5-6
3Rel	Religated	Inserted	ADP and ADP	6-7
4Rel	Religated	Inserted	empty and empty	~7

(Fig. 4A and Tables S1-S4). The residues identified in these dimer stabilizing regions are mostly consistent across configurations and studies [41,42]. In addition, the identified residues overlap with the those identified in the configurations simulated with a T-segment bound in the N-gate [42]. The overall strength of N-gate interactions was much lower in all configurations than what we observed for the DNA-gate and C-gate interactions, reflecting the dynamic nature of the N-gate compared to the more rigid properties of the remaining protein components involved in the capture and accommodation of the T-segment after being transferred through the DNA-gate.

The G-segment is firmly positioned within the DNA-gate, and free energy calculations indicate that favorably interacting residues are distributed throughout the gate (Tables S5-S8). Among these, positively charged residues—Arg475, Lys664, Arg650, Arg781, and Arg883—contribute most significantly. These residues are in the lower portion of the DNA-gate, which serves as the primary binding site for the G-segment. Individual residues from the K-loops of both protein chains formed by residues Ly333-Lys339 also contribute to the stabilization of the G-segment (e.g. Lys333). However, as we will discuss later, the overall contribution of each loop varies (Table S9). Such energetics

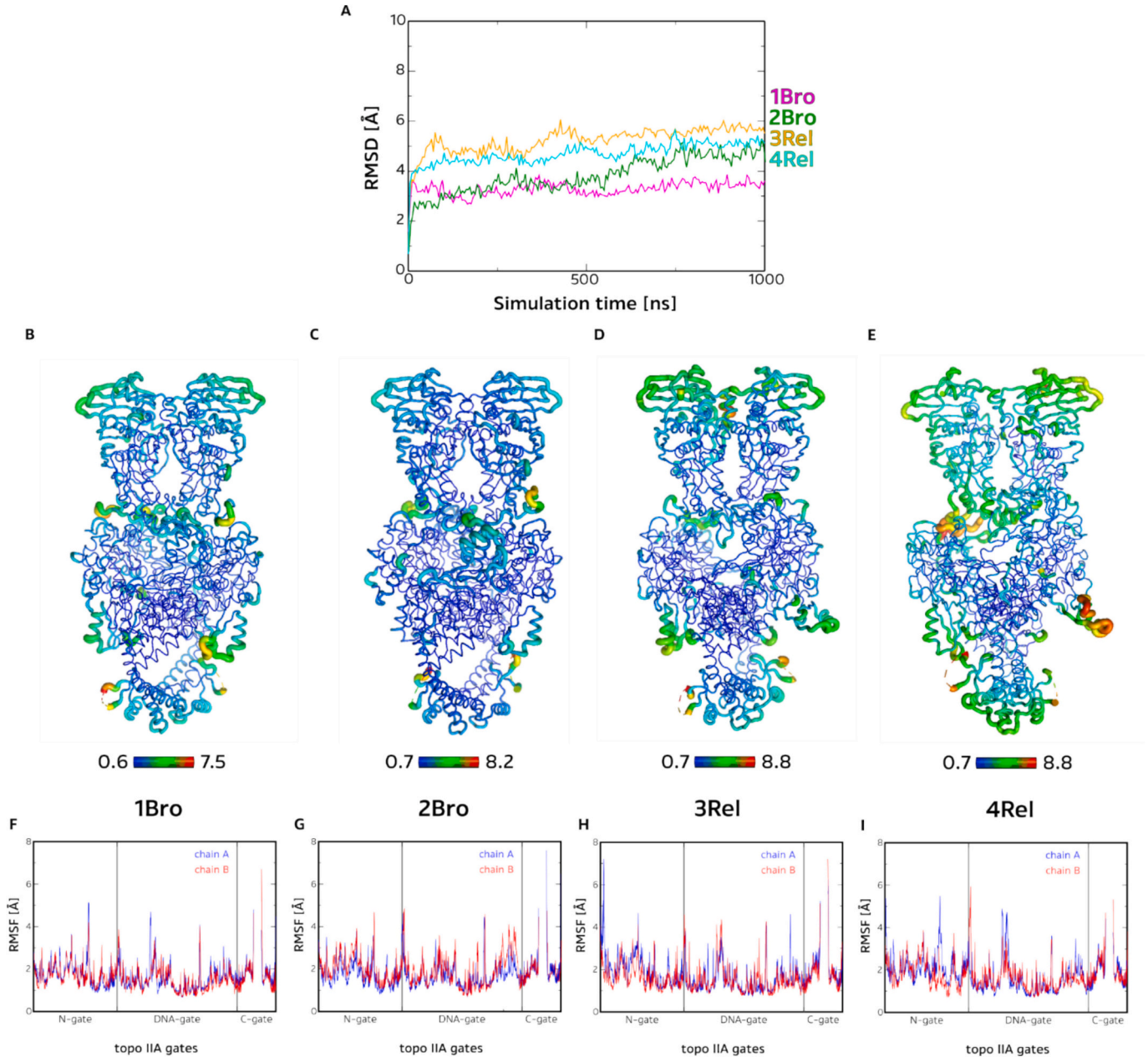

Fig. 3. (**A**) RMSD plots of simulated topo IIA configurations; (**B-E**) RMSF values displayed on topo IIA configurations with B-factors; (**F-I**) RMSF plots of topo IIA configurations with approximate labelled N-, DNA-, and C- gates.

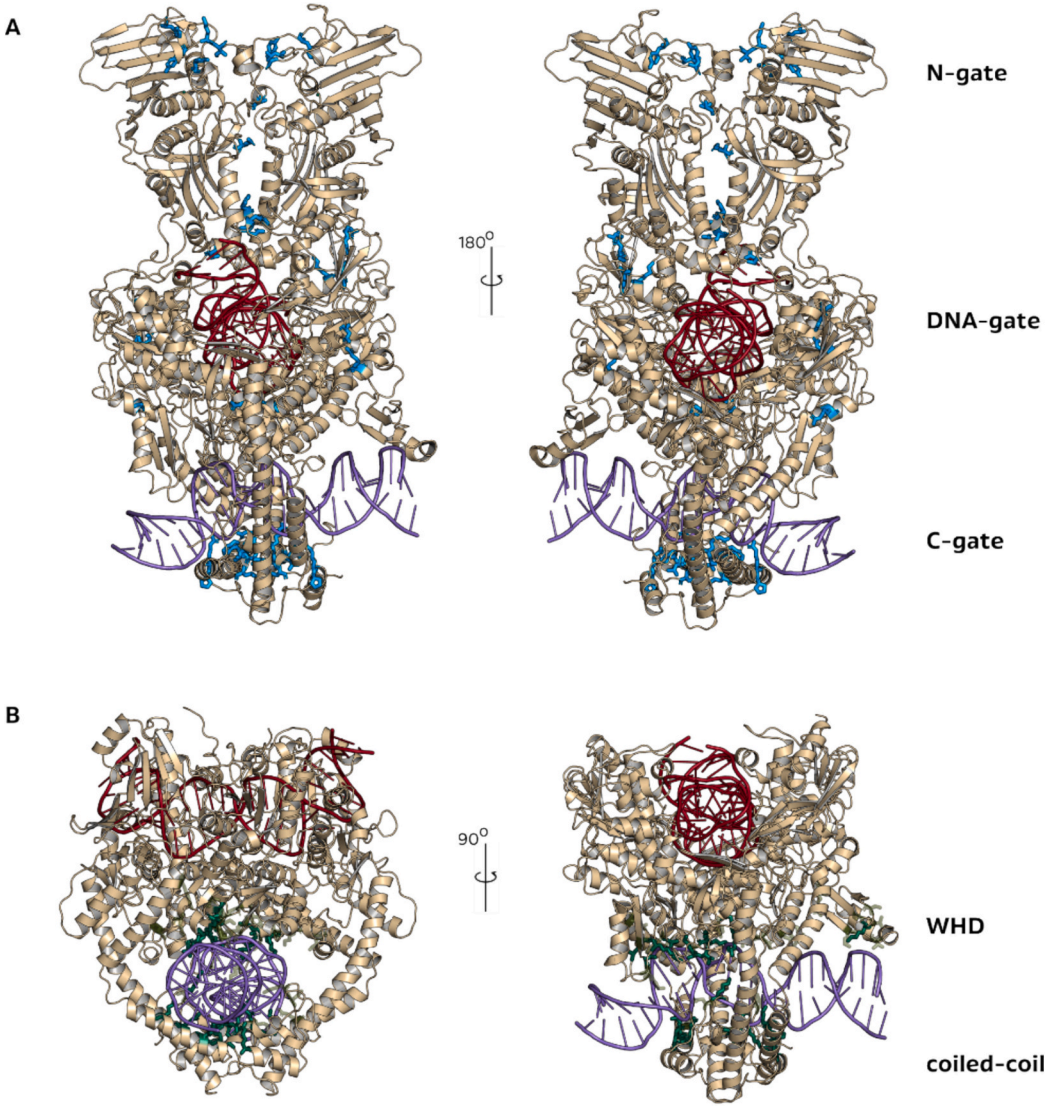

Fig. 4. **(A)** Results of free energy calculations exemplified on **4Rel** topo IIA configuration, with the marked residues (blue) forming the most favorable interactions between the dimers. Protein (beige), T-segment (violet), and G-segment (red). (**B**) Energetically most favorable interactive residues between topo IIA C-gate residues and T-segment depicted again on the **4Rel** configuration (light green – all important residues extracted from all four simulated topo IIA configurations dark green – energetically most favorable residues for this configuration). (For interpretation of the references to colour in this figure legend, the reader is referred to the web version of this article.)

between the G-segment and topo IIA are consistent with simulations in which the T-segment is present in the N-gate, indicating that its movement toward the C-gate does not significantly affect the G-segment stabilization.

In **1Bro** and **2Bro**, the residues stabilizing the G-segment are symmetrically distributed across the DNA-gate. Interestingly, in **3Rel** and **4Rel** systems, an additional favorable contribution emerges from residues in one monomer – Arg906 in **3Rel**, and even more prominently, Arg885 in **4Rel**. Geometric analysis of the trajectories revealed that both religated G-segment containing structures—particularly **4Rel**—exhibit greater tilting of the ATPase domains (Animation 1). This results in the asymmetric interactions of the G-segment with K-loops, with one loop being more engaged than the other. Thus, the additional interactions may act to compensate for this asymmetry, potentially stabilizing the DNA by balancing contacts on both sides of the gate.

Free energy calculations of the T-segment interacting with the C-gate revealed that its overall binding strength here was greater than when this DNA segment was present in the N-gate (Fig. 4B, Tables S10-S13) [42]. This suggests that as the T-segment transitions from the N-gate to the C-gate, it becomes more strongly bound. As with the G-segment, positively charged residues dominate the energetic landscape and contribute most significantly to the stabilization of the T-segment. The most energetically favorable anchor point is located at the end of the coiled-coil regions near the C-gate closure, with residues such as Arg1045, Lys1062, Arg1120, and Arg1128 playing key roles in binding. It was gratifying to observe that these residues had already been proposed—based on site-directed mutagenesis and biochemical studies—to act as a positively charged patch attracting the negatively charged T-segment [45], thereby corroborating our computational findings.

A second anchor point, also forming a positively charged interaction patch, is in the winged-helix domain (WHD) and includes residues Lys712, Lys713, Lys714, Lys716, Lys789, Lys793, Lys811, and Lys812. This observation aligns well with previous hypotheses that the basic region of the WHD forms a positively charged surface that helps to stabilize the T-segment after passage through the DNA-gate. Both patches likely contribute not only to stabilizing the T-segment but also to guiding it toward the exit from the C-gate.

Finally, we examined a flexible substructure of the TOPRIM domain,

which displayed notable conformational mobility and interacted with the T-segment. Here, residues Thr568, Thr569, Ly590, and Lys598 stood out but overall interactions of T-segment with this region were weaker than those at the two primary anchor sites. This suggests that, although the flexible TOPRIM section engages the T-segment more finely, it may play a role in fine-tuning its directional guidance during transport or in supporting its exit through the C-gate.

An additional key observation was that the relative strength of these interaction regions varied depending on the structural state, which could be connected with the asymmetric capture of the T-segment in the C-gate, being most pronounced in the **4Rel** structure. A recently reported crystal structure of the cleavage-core domain of African swine fever virus topoisomerase II showed the asymmetric binding of the T-segment [26], thus providing the experimental confirmation to our computational observations.

2.4. Essential dynamics reveal functionally coupled motions and allosteric communication across topo IIA domains

Structural studies on type IIA topoisomerases have shown that extensive conformational changes are required for the T-segment capture, its translocation through the C-gate, and its eventual release form the enzyme [15,46]. The performed molecular simulations are relatively long for systems of this size, yet they cannot capture these large-scale domain movements that typically occur on longer time scales. These transitions can be estimated by essential dynamics [47] to outline dominant collective motions and link them to the function of the molecular motor.

The principal component analysis (PCA) revealed several types of motion across all configurations (Figs. 5A-D, Fig. S4, and Animation 2). The observed movements are largely consistent with our previous study, implying them as inherent features of topo IIA mechanics and unaffected by the location of the T-segment. **1Bro** exhibited a gyration-like twisting motion in the first principal component (PC1), in which the DNA-gate residues and the N-gate elements, particularly of chain B, move in the opposing directions. The sliding motion in the DNA-gate, where structural elements in both chains move along the helical axis of the G-segment, was also detected. These features were assumed to represent integral features of topo IIA mechanics to enable the passage of the T-segment [42]. PC1 further captured the swinging movement in the lower C-gate residues as well as in the section of the TOPRIM residues 526-608, implicated in T-segment interaction. **2Bro** displayed a more pronounced tilting motion, with the N- and DNA-gate contacting elements of opposite chains approaching each other along with the sliding motion in the DNA gate (Animation 2).

The dominant feature of **3Rel** was the N-gate closure, characterized by the inward movement of the GHKL domains of both monomers, occurring early in the trajectory. PC1 motion corresponded to the asymmetrical closure of this domain, with one ATPase domain of the N-gate moving more prominently than the other. In addition, previously defined motions were also observed but with a smaller intensity. In **4Rel**, the twisting motion in the N-gate and sliding in the DNA-gate were again more pronounced. Additionally, increased movement was observed in TOPRIM residues 526-608, along with a more prominent

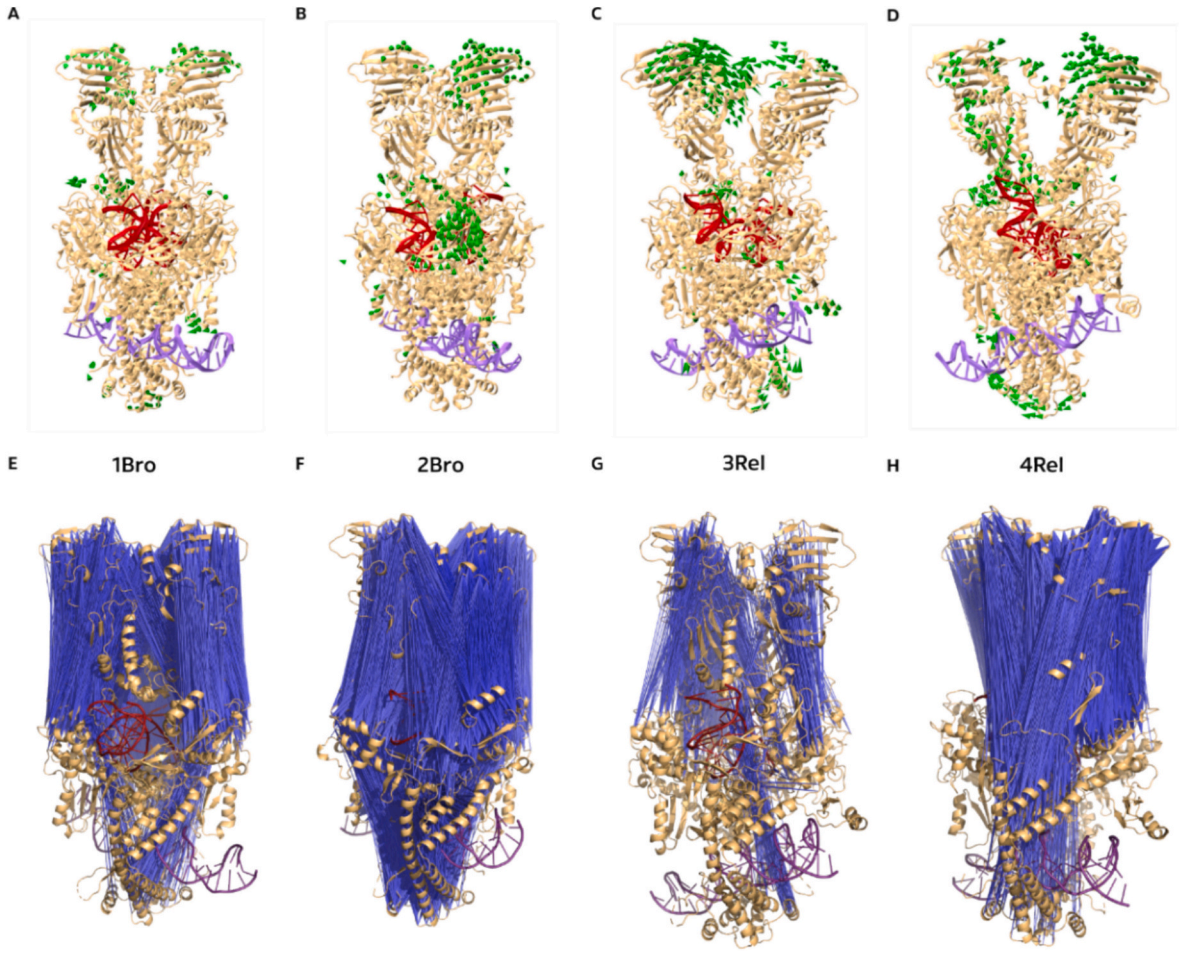

Fig. 5. Essential dynamics of the topo IIA with T-segment in the C-gate (**A-D**). Porcupine plots of PC1 showing the movement of residues larger than 3.0 Å in the simulated configurations (**E-H**). Pairs of residues displaying anti-correlations visualized on simulated structures. The pairs represent correlation coefficients ranging from −0.8 to −0.6. The positions of the Topo IIA chains are consistent with those shown in Fig. 1.

swinging motion of the C-gate (Animation 1). The second principal component (PC2) revealed gyration-like rotation in **1Bro**, whereas **2Bro** showed lateral N-gate twisting. In **3Rel** and **4Rel** configurations PC2 primarily described a swinging motion of the C-gate, coupled with either tilting in **3Rel** or twisting in the **4Rel** of the N-gate.

Analysis of replica simulations confirmed these dynamical features (Figs. S5-S6). Overall, the PC1 and PC2 predominantly captured twisting and tilting motions of the N-gate, often in combination with sliding of the DNA-gate along the helical axis of the G-segment. However, the relative dominance of these modes varied between replicas of the same configuration, likely reflecting differences in the conformational sampling. Generally, tilting of the N-gate became more pronounced in both configurations with a religated G-segment—especially in **4Rel**, where it is apparent even in visual inspection of the trajectory. This variability supports our earlier premise that gyration-like rotation and DNA-gate sliding are intrinsic dynamic features of topo IIA, expressed to different extents depending on the structural state [42]. In the absence of a T-segment in the N-gate, tilting also appears to be an important dynamic feature of the topo IIA dimer. By contrast, when bound in the N-gate conformational mobility of the ATPase dimer is constrained. Such tilting was observed experimentally in cryo-EM structures of human topo IIα in configurations lacking the T-segment in the N-gate [25].

Across all configurations—except to a lesser degree in **2Bro**—PC1 and PC2 consistently revealed a coupled motion involving the TOPRIM domain residues 526-608 and the C-gate. The subgroup of TOPRIM, interacts with the T-segment in the C-gate and appears highly flexible in all systems, supporting its role in coordinating C-gate dynamics with DNA processing. Importantly, neither direct trajectory visualization nor PCA in any system indicated any tendency toward a significant C-gate opening. These findings imply that this T-segment releasing step in the catalytic cycle cannot be significantly induced by G-segment religation, the nucleotide state (whether ATP or ADP is bound), or the presence of the T-segment in this gate alone.

To further characterize the essential motions, we calculated Dynamic Cross-Correlation Matrices, DCCM (Fig. S7). Residue pairs that exhibited the strongest correlated and anticorrelated motions were identified and mapped to their respective structures. As expected, strong correlated motions were observed primarily within individual subunits/domains, consistent with internal rigid-body-like dynamics (Fig. S8). In contrast, anticorrelated motions, typically indicative of the functionally relevant coupling between domains, offered mechanistic insights that complemented those obtained from PCA, further highlighting the dynamic interconnectivity of the molecular motor for successful function.

The N-gate and DNA-gate residues remained anticorrelated across all configurations, regardless of religation status of the G-segment or the presence/absence of nucleotide, emphasizing a persistent dynamic link between these domains which was observed in our previous configurations [42]. In addition, the some of the C-gate residues now occupied with the T-segment exhibited more intensive anticorrelations with the N-gate and DNA-gate as in previous configurations with the T-segment bound in the N-gate (Fig. 5E-H). Interestingly, despite this long-range communication, no significant internal anticorrelations were observed within the C-gate itself, suggesting a lack of intrinsic opening motion within the simulation timeframe, which is consistent with PCA findings.

Experimental studies with point mutations in the C-gate have shown that the modification of residues in this region can affect DNA cleavage activity [48]. In our simulations, the DNA cleavage step was not modeled directly, as these configurations represent the post-cleavage stages in which the T-segment is present in the C-gate. Nonetheless, essential dynamics, in particular the DCCM analysis, showed anticorrelated motions between the C-gate and DNA-gate residues, suggesting structural coupling. Introduced perturbations at the C-gate could propagate to the cleavage core, and possibly modulate catalytic activity, which could explain these experimental results.

Structure-specific differences in the DCCM patterns further supplemented our understanding of domain interactions. In **1Bro**, the DNA-gate of chain A—and to a lesser extent, chain B—exhibited anticorrelated motions with both chains of the N-gate (Fig. 5E). Additionally, the coiled-coil of chain B showed anti-correlations with both DNA and N-gates, whereas the coiled-coil of chain A primarily interacted with its own GHKL domain. In **2Bro**, additional anticorrelated motions were observed between the GHKL domain of chain B and the TOPRIM domains of both chains (Fig. 5F). The GHKL domain of chain B also displayed anti-correlations with the DNA-gate and the transducer domain of chain A, forming an extended interaction network that included the coiled-coil regions. These features show richer dynamic engagement of domains in **2Bro**, which is potentially linked to the hydrolysis of the remaining ATP molecule.

By contrast, the **3Rel** structure showed fewer anticorrelations overall, with most notable ones between the residues of the GHKL domain of chain A and the DNA-gate, TOPRIM, and coiled-coil regions of the same chain (Fig. 5G). Some intra-DNA-gate anticorrelations between the TOPRIM domains were also detected. In **4Rel**, anticorrelations were again more extensive. The GHKL domains of both chains were anticorrelated with the DNA-gate and the coiled-coil region of chain B comprising the C-gate. The transducer domains comprising the N-gate also showed anticorrelations with both the DNA-gate and the C-gate, as well as with the GHKL domain of chain B (Fig. 5H).

2.5. Nucleotide binding allosterically modulates topo IIA dynamics, while G- and T-segments asymmetrically interact with the topo IIA gates

After global topo IIA dynamics, we analyzed ATP and ADP molecules bound into the ATP binding sites. In all configurations, these nucleotides remained stably bound, with low RMSD values between 0.3 and 0.5 Å, even when the N-gate was adopted to open conformation (Figs. S9 and S10). This shows that ADP can persist in the nucleotide-binding pocket after γ-phosphate release and does not require a closed N-gate for retention.

In previous simulations where the T-segment was located in the N-gate [42], we observed interactions between the ADP and the QTK loops, which are proposed to mediate communication between the N-gate and the DNA-gate [49,50]. In the current set of topo IIA configurations these interactions varied by system. In **1Bro**, ATP engaged the QTK loop as expected, while ADP in the opposite site adopted a similar orientation but did not form interactions with the loop. Distance analyses and MM/GBSA calculations both confirmed minimal energetic contributions from the QTK residues in this system (Table 2). Replicas were consistent with these findings, although one showed the ADP ligand becoming less stable, suggesting a potential for dissociation.

In **2Bro**, the ADPs mostly did not contact the QTK loop, however one replica exhibited QTK interaction with one of the ADP molecules. This interaction was even more pronounced in **3Rel**, where the N-gate was initially open (Fig. 6A). In the original run and the two replicas, one ADP molecule fully engaged the QTK loop, while the other remained bound but not interacting with it. These observations indicate that after ATP is hydrolyzed, ADP can participate in QTK loop interactions, particularly when the N-gate is open. This supports the premise that nucleotide occupancy plays an allosteric role in modulating N-gate conformation and suggests that ADP dissociation may be required to facilitate full N-gate opening [42].

To further evaluate these observations MM/GBSA free energy calculations estimated the binding energetics (Tables 2 and S14). As expected, ADP exhibited weaker overall binding free energy compared to ATP. The residues contributing favorably to binding were consistent with previous studies [42]. The adenine moiety was the most lightly bound, while the ribose was stabilized primarily by Ser127, Ser128, and Asn129. The phosphate groups favorably interacted with residues between Gly140 and Lys147, with Lys147 again emerging as one of the key contributors to ligand binding across all configurations. Lys147 appears to act as the main anchor of ADP and ATP, most probably enabling the ADP prolonged residence time in the ATP binding site. In light of this the

Table 2
Per-residue decomposition of the binding free energy of the ATP/ADP ligands and ATP binding site residues in topo IIA configurations.*

Protein chain	Residues	Energy 1Bro [kcal mol^{-1}]	Energy 2Bro [kcal mol^{-1}]	Energy 3Rel [kcal mol^{-1}]
	Asn70	-4.4 ± 1.5	-0.4 ± 1.5	-3.6 ± 1.4
	Ser127	-9.1 ± 1.1	-1.0 ± 0.5	-8.3 ± 1.3
	Ser128	-1.8 ± 0.9	-7.1 ± 2.8	-3.0 ± 1.0
	Asn129	-9.5 ± 2.5	-0.8 ± 0.9	-3.9 ± 2.8
	Gly140	-7.1 ± 1.0	-2.3 ± 2.5	-7.4 ± 0.6
	Arg141	-8.1 ± 1.6	-6.0 ± 1.8	-7.8 ± 0.8
CHAIN A	**Asn142**	-8.0 ± 1.9	-7.5 ± 2.6	-8.6 ± 1.5
	Gly143	-8.2 ± 0.9	-9.5 ± 1.2	-7.5 ± 0.9
	Tyr144	-2.4 ± 0.7	-7.9 ± 1.5	-2.2 ± 0.7
	Gly145	-3.6 ± 0.9	-8.4 ± 1.0	-4.9 ± 0.8
	Ala146	-4.3 ± 0.8	-4.9 ± 0.5	-4.5 ± 0.6
	Lys147	-20.8 ± 1.5	-20.9 ± 3.1	-20.7 ± 2.0
	Lys367	-1.7 ± 0.5	-2.8 ± 1.1	-3.0 ± 0.8
	Asn70	-1.3 ± 1.4	-5.0 ± 1.2	-3.5 ± 1.2
	Ser127	-6.3 ± 1.0	-8.7 ± 1.3	-7.0 ± 1.0
	Ser128	-2.5 ± 0.8	-2.8 ± 1.4	-2.6 ± 0.9
	Asn129	-6.7 ± 1.2	-5.2 ± 3.1	-4.3 ± 0.8
	Gly140	-7.9 ± 0.7	-5.9 ± 1.1	-7.9 ± 0.7
	Arg141	-9.3 ± 0.9	-6.6 ± 1.6	-8.4 ± 0.7
CHAIN B	**Asn142**	-11.8 ± 2.3	-8.8 ± 1.4	-8.1 ± 1.0
	Gly143	-7.9 ± 1.2	-8.9 ± 0.9	-6.3 ± 0.8
	Tyr144	-8.6 ± 0.9	-2.6 ± 0.9	-3.0 ± 0.7
	Gly145	-7.8 ± 1.0	-4.2 ± 0.8	-6.6 ± 0.7
	Ala146	-4.2 ± 0.6	-4.8 ± 0.6	-4.1 ± 0.6
	Lys147	-19.4 ± 2.0	-20.5 ± 1.9	-21.3 ± 1.8
	Lys367	-20.9 ± 2.0	-0.1 ± 0.1	-21.8 ± 2.0

* In **1Bro** ATP is bound to chain B, while ADP is bound to chain A.

determined posttranslational modification of this residue appears very reasonable mechanism of control of this molecular motor [30]. Finally, Lys367 showed comparable energetic contribution over all configurations, in cases where interactions with the QTK loop were observed.

In the further assessment of the N-gate dynamics, we monitored the distances between QTK loops as well as between the centers of mass of the GHKL domains. We focused particularly on the G-segment religated configurations where the N-gate was initially left open to further probe the allosteric role of the ADP. Average distances were 13.2, 13.4, 14.6, and 17.4 Å for **1Bro, 2Bro**, **3Rel**, and **4Rel**, respectively; while the corresponding distances between the GHKL domains were 37.2, 37.3, 38.1, and 40.5 Å (Tables S15-S17).

In all simulations of **1Bro** and **2Bro**, the N-gate remained stably closed, consistent with the presence of ATP or ADP in the binding sites. In contrast, the **3Rel** structure containing two ADPs showed spontaneous N-gate closure early in the simulation, a behavior observed also in both replicas. This further supports a stabilizing role for ADP in maintaining the closed conformation. In **4Rel,** where both ATP binding sites were unoccupied, the N-gate remained predominantly open despite a brief narrowing. The two replicas diverged: one maintained the open state, while the other sampled a partially closed conformation. This likely reflects the increased flexibility of these nucleotide-free topo IIA configurations and suggests that multiple conformations are accessible which is favorable for the release of the G-segment (Figs. S11-S15).

Given the observed N-gate closure in the **3Rel,** we further analyzed the trajectory by dividing it into two segments: before and after the N-gate closure. While the first part captures the dynamics associated with closure, the second segment, with the N-gate closed, resembles the dynamic behavior observed in the **1Bro** and **2Bro** configurations. The RMSF analysis shows a clear reduction in the overall flexibility after closure (Fig. S16). Although most regions of the protein with increased dynamics remained the same, their amplitudes decreased significantly in the second part of the trajectory, indicating a global structural stabilization. Before closure, the GHKL domain of chain A exhibited increased flexibility, while chain B remained relatively rigid. Surprisingly, the ADP on the more flexible side in all three replicas did not interact with the QTK loop, suggesting a link between nucleotide interaction and domain mobility while the other ADP always engaged the QTK loop. PCA confirmed this asymmetry: in the pre-closure stage, PC1 noted a concerted movement dominated by the GHKL domain of chain A, while chain B remained static (Fig. S17). After closure, PC1 described a rotational movement reminiscent of **4Rel.** Cross-correlation analysis was consistent with these results, showing strong anti-correlations between the GHKL domain of chain A and the DNA- and C-gates in the pre-closure stage, consistent with large-scale rearrangements between the domains (Fig. S18). In contrast, anticorrelations in the post-closure part were much weaker and occurring only in the DNA and N-gate. These results suggest that N-gate closure could be driven by rather asymmetric dynamics of the N-gate associated with subsequent reduced flexibility and communication between domains.

To further explore the asymmetry observed for the binding of the G-segment in the DNA-gate in free energy calculations (Table S9), we examined the average distances between the centers of mass of each chain's K-loop and the G-segment. K-loops are known to play a key role in coupling G-segment binding to ATPase activity [19], and simulations revealed a consistent degree of asynchrony. In all configurations, the K-loop from one chain is placed closer to the G-segment than in the other, however the degree varies. Interestingly, in **1Bro** and **2Bro** it is the chain B that engages the G-segment more while this is reversed for the **3Rel** and **4Rel** configurations. Revealing both orientations as possible in the topo IIA dimer (Table 3 and Fig. S19).

This asymmetry is particularly pronounced in **4Rel**, where the K-loop of chain A aligns closely with the G-segment, while the K-loop of chain B remains more distant (Fig. 6C). Correspondingly, the hydrogen bonding between chain B's K-loop and the G-segment is minimal here (Tables S18-S19). MM/GBSA free energy decomposition further showed that the energetic contributions of K-loop Lys residues indicate unequal stabilization of the G-segment, which is especially evident in **4Rel** (Table S9). This asymmetric K-loop engagement prompted us to explore whether a tilting motion of the G-segment—previously proposed in early simulations of the catalytic cycle and supported by experimental cryo-EM data for human topo IIα—might be observed. Indeed, in **4Rel**, the G-segment exhibits a pronounced tilt toward the more engaged K-loop (Animation 1), indicating an allosteric coupling between K-loop positioning and DNA handling at the G-segment.

To further describe the asymmetric binding of the T-segment within the C-gate (Fig. 7A-B), we defined directional distance vectors between the center of mass of the central T-segment region and specific protein regions implicated in key interactions. These regions were identified based on residues with significant energetic contributions to T-segment stabilization across all four configurations as determined by MM/GBSA analysis. Residues were grouped into four interaction zones: one winged-helix domain (WHD) and one shared region within the coiled-coil arms per monomer. The WHD zones included Lys712, Lys713, Lys714, Lys716, Tyr727, Lys789, Lys793, Lys811, and Lys812, while the coiled-coil interaction zone comprised Arg1045, Asn1061, Lys1062, Met1083, Arg1084, Arg1092, Lys1095, Gln1099, Lys1103, and Arg1136. Residues from the flexible portion of the TOPRIM domain were excluded to focus the analysis on the structurally constrained cavity formed by the DNA- and C-gates. For the T-segment, we defined its central six base pairs as the core, enabling consistent vector-based comparisons across all simulations (Fig. S20-S21).

Geometric analysis revealed a clear directional asymmetry in the T-segment positioning within the C-gate. In **1Bro** and **2Bro,** the distances between the T-segment core and the WHD and coiled-coil regions of chain A were approximately 15–16 Å and 13–14 Å, respectively, while corresponding distances for chain B were 18–19 Å and 15–16 Å (Fig. 7B and Table 4). In contrast, **3Rel** and **4Rel** displayed the opposite asymmetry, reflecting a reproducible shift in T-segment positioning linked to altered K-loop–G-segment interactions (Fig. 6C). This structural asymmetry complements the observed energetic difference from MM/GBSA calculations and provides a mechanistic rationale for the asymmetric

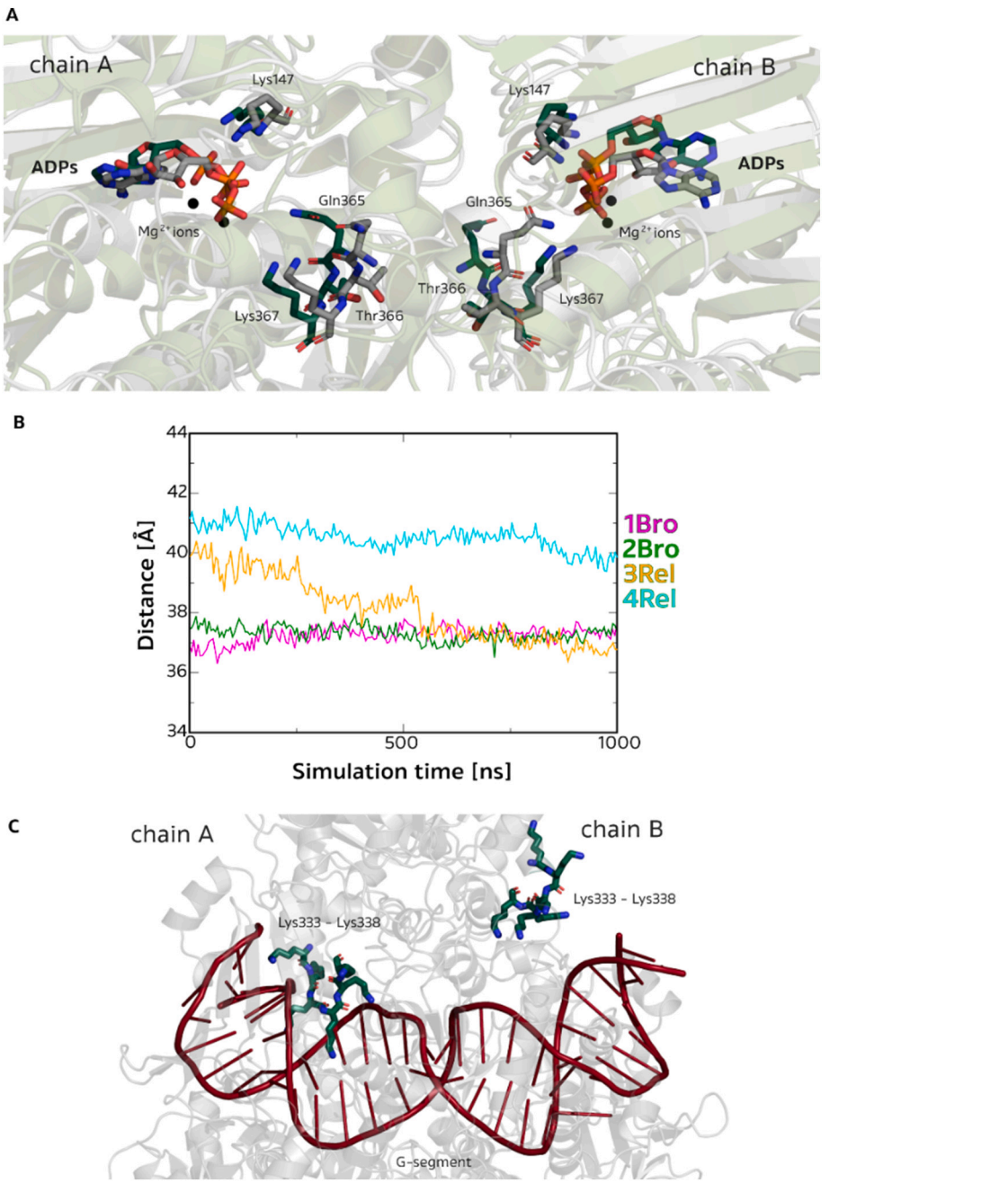

Fig. 6. Dynamics of the key elements of topo IIA configurations. **(A)** Interactions between ADP molecules (orange) and QTK loops of **2Bro** (dark blue) and **3Rel** topo IIA (gray). **(B)** Distances between the centers of mass of the ATPase domains of both chains. **(C)** Asymmetric position of K-loops and DNA G-segment exemplified by **4Rel.** (For interpretation of the references to colour in this figure legend, the reader is referred to the web version of this article.)

Table 3
The average distances between the center of mass of each K-loop and the G-segment of each simulated topo IIA configuration.

K-loop: G-segment distance	1Bro [Å]	2Bro [Å]	3Rel [Å]	4Rel [Å]
Chain A	24.1 ± 0.9	24.5 ± 1.2	16.7 ± 1.6	18.3 ± 1.2
Chain B	20.0 ± 1.2	16.8 ± 0.7	24.7 ± 0.7	27.3 ± 1.7

engagement of the T-segment at the C-gate.

To further investigate the dynamics of the C-gate, we performed a principal component analysis considering only the C-gate residues. In all configurations the PC1 showed that the C-gate exhibited significantly less flexibility compared to the N-gate. The predominant motions were localized in the upper part of the coiled-coil domain along with subtle motions at the C-gate interface, mainly in the form of slight sliding motions (Fig. 7C). Importantly, no motions reminiscent of the "book-like" opening of the C-gate were observed. Even in the presence of the bound T-segment, the C-gate thus remained dynamically constrained. These findings suggest, full opening of the C-gate likely requires a preceding conformational change, possibly triggered by a release of the G-

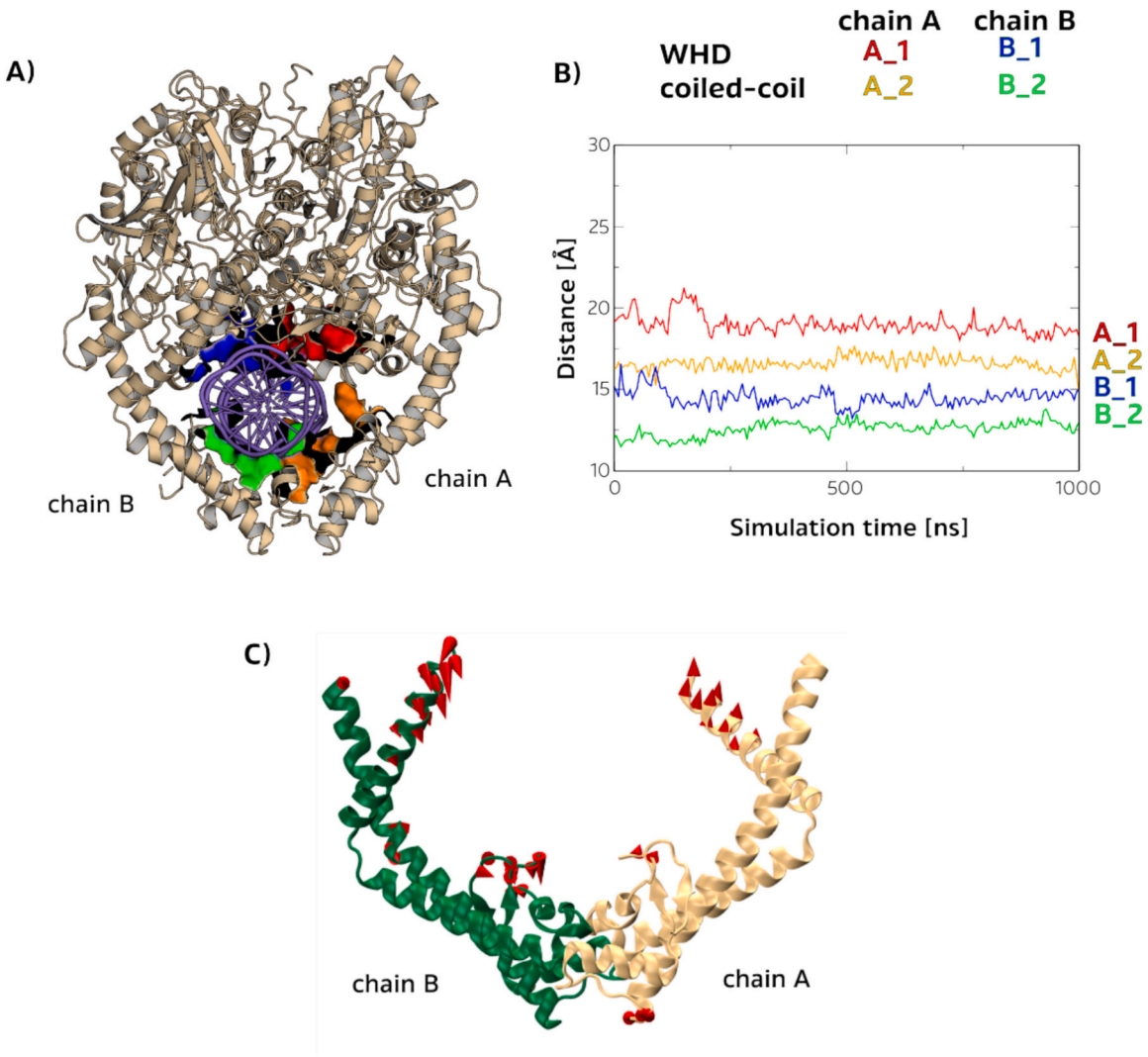

Fig. 7. Dynamics of the topo IIA C-gate. (**A-B**) Defined regions on the WHD and coiled-coil domains of **4Rel** that served as starting points to define directional distance vectors between the center of mass of the central T-segment region and selected C-gate protein regions. WHDs in chain A and B are shown in red and blue, while coiled-coil regions are shown in orange and green for chain A and B, respectively. (**C**) Local PCA analyses of the C-gate residues. Porcupine plots of PC1 showing the movement of residues in **4Rel** larger than 2.0 Å in the simulated configurations. (For interpretation of the references to colour in this figure legend, the reader is referred to the web version of this article.)

Table 4
Average distances between the selected regions in the WHD domain or the shared region within the coiled-coil domain and the T-segment across all simulated topo IIA configurations.

Chain	C-gate:T-segment distance	1Bro [Å]	2Bro [Å]	3Rel [Å]	4Rel [Å]
Chain A	WHD	15.1 ± 0.5	16.1 ± 0.5	19.3 ± 0.9	19.0 ± 0.6
	Coiled-coil	12.6 ± 0.2	14.4 ± 0.9	17.0 ± 0.7	16.6 ± 0.4
Chain B	WHD	18.1 ± 0.5	16.9 ± 0.8	13.5 ± 0.5	14.5 ± 0.5
	Coiled-coil	16.0 ± 0.7	17.5 ± 0.7	12.9 ± 0.8	12.6 ± 0.5

segment and reopening of the N-gate.

2.6. Presence of the T-segment in the C-gate influences bending of the G-segment

The DNA representing both the T- and G-segments was modeled with an identical palindromic sequence (Fig. 8A-B). The T-segment, located in the C-gate, is subject to fewer spatial constraints as the available cavity provides ample space for conformational flexibility. In contrast, the G-segment within the DNA-gate is more constrained. Quantitative analysis of DNA bending revealed that in the presence of a T-segment bound to the C-gate, the G-segment adopts a much more extended conformation, which differs significantly from the configurations in which the T-segment is located in the N-gate. The average total bending angles of the G-segment in **1Cle**, **2Cle**, and **3Rel** were measured to be 169.8 ± 5.4°, 171.9 ± 4.4° and 170.6 ± 5.1°, respectively (Fig. 8C). These values indicate a pronounced straightening of the DNA after passage of the T-segment through the cleavage complex. In comparison, when the T-segment was positioned in the N-gate, the G-segment exhibited significantly greater curvature, with bending angles between

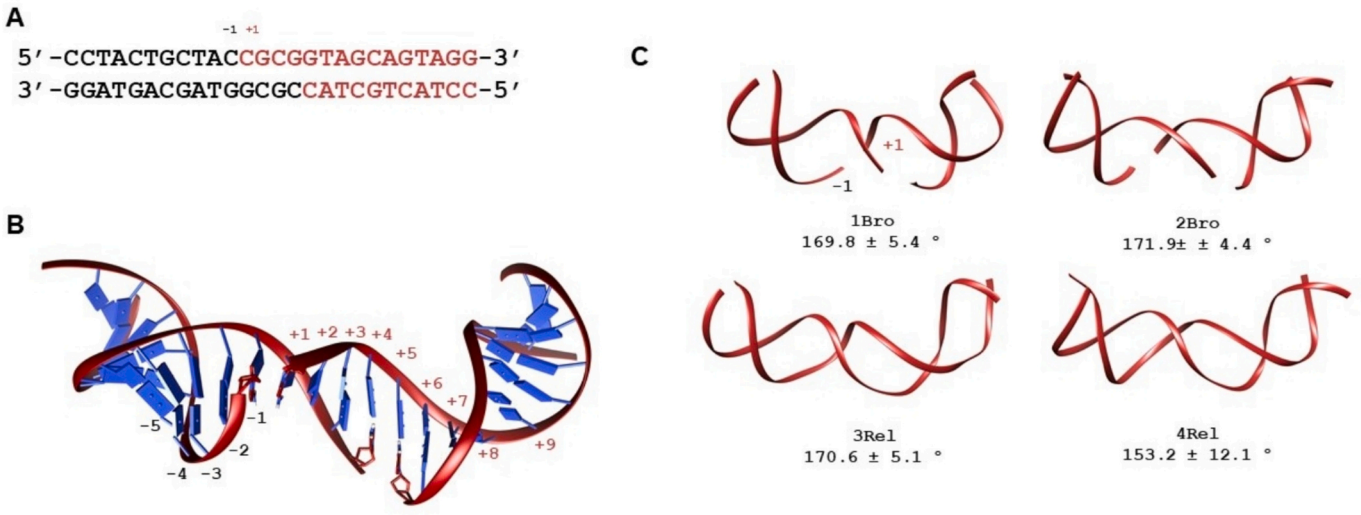

Fig. 8. (**A**) Nucleotide sequence of the G- and T-segments used in the simulations, with the cleavage site highlighted in case of G-segment. (**B**) 3D representation of the DNA with base pairs marked (**C**) Average bending angles of the G-segment in the **1Bro**, **2Bro**, **3Rel**, and **4Rel** configurations; the mean curvature values together with standard deviations are indicated below each structure.

Table 5
x-displacement parameters for the DNA base pairs from the G-segment DNA base pairs from −5 to +9 for the simulated topo IIA systems along with the initial structure from our previous study. Red colored cells represent the B-DNA conformation, the blue ones the A-DNA, and the gray ones the conformation between A- and B-DNA. The x-displacement parameter has a value of −4.17 ± 1.22 Å and 0.05 ± 1.28 for A- and B-DNA, respectively.

x-displacement base pair no.	1Bro [Å]	2Bro [Å]	3Rel [Å]	4Rel [Å]	Cleaved* [Å]	2Pre** [Å]
-5	0.22 ± 1.01	−0.05 ± 0.81	−1.09 ± 0.80	−0.99 ± 0.80	−1.24 ± 0.62	−1.83 ± 0.54
−4	−0.33 ± 0.69	−0.27 ± 0.69	−0.07 ± 0.76	0.00 ± 0.69	−1.41 ± 0.56	−1.47 ± 0.49
−3	−0.10 ± 0.49	−0.09 ± 0.52	−0.32 ± 0.91	−0.49 ± 0.72	−2.92 ± 0.56	−2.95 ± 0.52
−2	0.01 ± 0.39	−0.05 ± 0.43	−0.22 ± 0.91	−0.15 ± 0.96	−3.07 ± 0.60	−2.99 ± 0.59
−1	0.50 ± 0.56	−0.03 ± 0.53	−0.45 ± 1.05	−0.05 ± 1.01	−4.52 ± 0.87	−3.18 ± 0.55
+1	0.40 ± 0.59	0.01 ± 0.71	−0.15 ± 0.77	−0.41 ± 0.48	−3.80 ± 0.68	−3.25 ± 0.56
+2	0.17 ± 0.92	−0.30 ± 1.08	−0.06 ± 0.93	−0.21 ± 0.64	−4.63 ± 0.72	−3.51 ± 0.54
+3	−0.18 ± 0.92	0.33 ± 1.03	−0.19 ± 0.86	−0.22 ± 0.61	−4.35 ± 0.61	−2.75 ± 0.61
+4	−0.21 ± 0.55	−0.15 ± 0.74	−0.14 ± 0.57	−0.12 ± 0.42	−3.58 ± 0.55	−3.41 ± 0.57
+5	−0.01 ± 0.42	0.01 ± 0.49	−0.07 ± 0.44	−0.02 ± 0.49	−4.77 ± 0.49	−1.60 ± 1.23
+6	0.14 ± 0.44	0.14 ± 0.41	0.17 ± 0.51	0.13 ± 0.50	−2.60 ± 0.61	−1.61 ± 1.01
+7	0.00 ± 0.54	0.07 ± 0.56	−0.12 ± 0.79	−0.15 ± 0.71	−2.67 ± 0.55	−2.07 ± 1.34
+8	0.21 ± 0.60	0.21 ± 0.63	0.48 ± 0.79	0.32 ± 0.64	−1.27 ± 0.62	−2.17 ± 0.75
+9	−0.06 ± 0.71	0.11 ± 0.64	0.11 ± 0.81	0.61 ± 0.73	−1.37 ± 0.54	−2.40 ± 0.60

* published in Ref. 41.
** published in Ref 42.

100° and 125° [42]. Even in systems where only the G-segment was bound and no T-segment was present, the bending angles remained lower, typically between 110° and 120° [41], suggesting that the conformational state of the G-segment is very sensitive to the presence and position of the T-segment. In **4Rel**, the G-segment showed a partially recurved conformation with an average bend angle of 153.2 ± 12.1°, which is very similar to the previously reported value of 156.6 ± 12.8° for the free G-segment simulation [41]. This partial recovery of curvature could reflect a transient intermediate state prior to release. Furthermore, the standard deviations of the bending angles in systems **1Bro**, **2Bro**, and **3Rel** were relatively small, indicating a stable DNA conformation under these conditions. In contrast, system **4Rel** exhibited a higher standard deviation (12.1°), indicating increased flexibility, similar to what was observed in both free DNA and previous simulations of the G-segment alone.

To further characterize the conformations of the G-segments, we calculated structural parameters such as x-displacement and slide, which indicate the helical shape of the DNA. These parameters are commonly used to distinguish between A- and B-DNA conformations [51]. The x-displacement is a global helical parameter that describes how far a base pair is shifted along the x-axis of the helical coordinate system compared to ideal B-DNA. Characteristic values for the x-displacement values are −4.17 ± 1.22 Å for A-DNA and 0.05 ± 1.28 Å for B-DNA. In all four simulated configurations including replicas, the G-segment consistently adopted values close to those of canonical B-DNA, indicating the preservation of this helical form throughout the simulations. A similar trend was observed for the slide parameter, which measures the relative displacement between neighboring base pairs along the axis that is perpendicular to both the helical axis and the base pair plane. Although the differences in slide values were less pronounced than for the x-displacement, they still supported the predominance of a B-DNA-like conformation [51]. These observations are summarized in Table 5, with additional data provided in Tables S20–S21 and Figs. S22–S23.

Interestingly, in systems where no T-segment was present either in C-gate or N-gate there was a broader distribution of A-DNA-like features, particularly in regions proximal to the cleavage site. This suggests that DNA compression into an A-like form may be a preparatory step in the catalytic cycle, potentially facilitating strand cleavage or bending. Importantly, the presence or absence of ADP/ATP did not appear to

influence G-segment topology, reinforcing the idea that the significant changes in DNA conformation are driven by T-segment binding events. Taken together, these results support a model in which G-segment topology is dynamically modulated during the initial stages of the catalytic cycle, prior to and possibly facilitating T-segment passage.

3. Discussion

Our comprehensive molecular dynamics simulations provide mechanistic insight into the stages of the catalytic cycle of yeast type IIA topoisomers following transport of the T-segment, corresponding to *Structures 5–7* shown in Fig. 1. Placement of the T-segment in the C-gate required far fewer structural manipulations than insertion into the N-gate, making these configurations even more realistic approximations. By integrating the simulation results with the available biochemical data, approximations, we can extend our understanding of the catalytic cycle.

3.1. ATP and ADP as modulators of the N-gate dynamics

The N-gate dynamics are crucial for T-segment capture and subsequent G-segment release. Our simulations show that both ATP and ADP stabilize the closed N-gate conformation, even in the absence of a bound T-segment. In particular, the **3Rel** system with ADP/ADP nucleotides, started with an open N-gate, rapidly adopted and maintained a closed conformation in all replicas. This indicates that ADP actively stabilizes N-gate closure even after T-segment transport and G-segment religation. In contrast, the **4Rel**, lacking the bound nucleotides, maintained an open or partially closed N-gate and exhibited greater degree of conformational variability– a prerequisite for the final G-segment release later in the catalytic cycle. These observations are further supported by global dynamics (e.g., RMSD) and interdomain distances (e.g., GHKL and QTK loop separations), where ATP/ADP-bound systems **1Bro, 2Bro, 3Rel** featured a consistently closed N-gate, while **4Rel** displayed larger average N-gate dimensions and increased flexibility.

The interaction between nucleotides and the QTK loop is a known communication axis linking the ATPase site to the DNA-gate [49]. In **1Bro**, ATP engaged the QTK loop as expected. In **1Bro** and **2Bro** (ADP sites), interactions involving ADP were more variable. Notably, in **3Rel**, one ADP molecule consistently interacted with the QTK loop on the same chain across all three replicas. This interaction agreed with asymmetric N-gate closure, suggesting a continued allosteric influence of ADP on domain dynamics even after the T-segment passage.

The stable binding of ADP, particularly via anchoring residues like Lys147, may prolong its presence in the binding pocket and allow it to exert continued allosteric effects. Its eventual dissociation likely serves as the trigger for sustained N-gate opening and G-segment release. In the closely related human topo IIα, the activity of the enzyme is regulated by a posttranslational modification - the acetylation of the corresponding Lys168 residue [30]. This modification neutralizes the positive charge of the lysine side chain and introduces steric hindrances that weaken the interactions of the nucleotides with the ATP binding pocket. Our simulations corroborate this, as Lys147 was found to be a key energetic residue involved in the binding of both nucleotides, likely also regulating N-gate dynamics and preventing premature dissociation of the G-segment even in the late stages of the catalytic cycle and thus the occurrence of DNA double-strand breaks. While the precise functional consequences of ADP binding interactions warrant further investigation, our simulations clearly support a role for ADP as an allosteric modulator of N-gate dynamics also after T-segment passage.

The kinetic evaluation of ATP hydrolysis in topo IIA has shown that the hydrolysis of the two bound ATP molecules proceeds sequentially and that phosphate and ADP are released after the first hydrolysis, and that the transport of the T-segment occurs before the hydrolysis of the second ATP [35]. In our previous set of topo IIA configurations with the T-segment in the N-gate, we also included a configuration in which one ATP molecule was bound while the second site was empty. Overall, we observed the widening of the N-gate with decreasing nucleotide occupancy, confirming allosteric regulation during T-segment capture [42]. For the current topo IIA configurations with the T-segment in the C-gate, a similar trend in allosteric modulation of the N-gate by nucleotides was observed, together with comparable dynamics and behavior of the DNA-gate and C-gate across all simulated cases. These results suggest that modeling of a single-ATP state could provide additional mechanistic detail but would not significantly alter our overall conclusions.

3.2. Asymmetric T-segment binding in the C-gate modulates G-segment topology and influences inter-gate communication

Following the passage through the DNA-gate, the T-segment is temporarily retained within the C-gate prior to final release. Our simulations provide new insights into the nature of T-segment binding in this region, the asymmetry of its positioning, and the structural dynamics of the C-gate itself.

Binding free energy calculations indicate that binding of the T-segment in the C-gate is energetically favorable, supporting the idea of a secure handoff mechanism and electrostatic stabilization prior to release. However, these energetic results should be interpreted qualitatively given the known limitations of the MM/GBSA approach in estimating binding affinities. Positively charged residues play a central role in this process, attracting and guiding the T-segment as it moves through the DNA-gate. Two primary anchor points were identified: a positively charged patch at the base of the coiled-coil helices near the gate exit (e.g., Arg1045, Lys1062, Arg1120, Arg1128), and a second patch within the winged-helix domains (WHDs), involving residues Lys712, Lys713, and Lys811-812. These results are consistent with experimental evidence implicating involvement of both regions in T-segment retention [45].

The T-segment exhibited asymmetric binding within the C-gate, with its position shifting depending on the structural state. In **1Bro** and **2Bro**, it was preferentially positioned closer to chain A's coiled-coil and WHD elements, whereas in **3Rel** and **4Rel** the interaction shifted toward chain B. This asymmetry was supported by interaction energy profiles and center-of-mass distance analyses. The trend mirrors a recent crystal structure of the African swine fever virus topoisomerase II, which also displayed asymmetric T-segment placement in the C-gate. Our simulations further show that this asymmetry is preserved even in the presence of a closed N-gate, indicating a persistent directional bias [26]. The observed asymmetric T-segment binding may, potentially enable one-sided detachment or a directional sliding mechanism through the C-gate. Interestingly, these asymmetric interactions were echoed in K-loop–G-segment interactions, which displayed complementary chain preferences—favoring chain B in **1Bro**/**2Bro** and chain A in **3Rel**/**4Rel**. In **4Rel**, this bias was especially pronounced and coincided with a N-gate tilt toward the more engaged K-loop (Animation 1) which was also observed experimentally [25].

The dynamics of the flexible TOPRIM segment comprised of an α-helix and three β-sheet substructures, observed in our previous studies, was here put to functional context due to its transient contacts with the T-segment via residues such as Thr568, Lys590, and Lys598. While these interactions were weaker, PCA revealed coordinated motions between this protein segment and the coiled-coil helices of the C-gate (except for **2Bro**), suggesting that its flexibility may assist in fine-tuning T-segment positioning or guiding its exit.

Despite T-segment occupancy, the C-gate remained principally closed throughout the simulations. PCA focusing on C-gate residues revealed limited essential dynamics restricted to small local displacements, with no evidence of large-scale opening conformations. DCCM analysis similarly showed no significant internal anti-correlations indicative of C-gate opening propensity. This rigidity contrasts with significant dynamic behavior at N-gate (see Section 3.3) and highlights the C-gate's function as a retention site rather than an active exit point

during these stages. However, the increased occurrence of anti-correlations between the C-gate and the N-/DNA-gates in the new set of configurations suggest a system-spanning allosteric network, where mechanical coupling between G-segment and downstream C-gate rearrangements might be required to facilitate eventual T-segment release.

Notably, the positioning of the T-segment within the enzyme also exerted a profound effect on the conformation of the G-segment. When the T-segment was bound within the C-gate cavity, the G-segment exhibited significantly straighter geometries, with average bending angles consistently near 170°, in contrast to much more curved conformations (100°-125°) observed in earlier catalytic states where the T-segment resided in the N-gate or was absent [41]. In the **4Rel** configuration, the G-segment displayed an intermediate bend (around 153°), likely reflecting a transient state prior to full release. These observations highlight the functional interdependence of the two DNA segments across catalytic states. These findings support the notion that T-segment occupancy mechanically assists G-segment straightening, facilitating religation and preparing the enzyme for reset.

Complementary helical parameter analysis revealed that the G-segment retained a predominantly B-DNA-like topology across all late-stage configurations. However, subtle transition toward A-like geometries was observed when no T-segment was bound, particularly near the cleavage site. This observation strengthens the hypothesis that A-form-like bending may prepare the G-segment for cleavage earlier in the cycle, while B-form straightening facilitates religation and release. Together, these results highlight the interdependence of the DNA segments across catalytic states and show that asymmetric T-segment retention modulates both DNA topology and gate dynamics.

3.3. Coordinated gate transitions and allosteric coupling orchestrate the final DNA release events

The catalytic cycle of type IIA topoisomerases concludes with the G-segment religation and release of DNA segments and ADP molecules, simplifying the DNA topology and resetting the enzyme. Our simulations, which studied the topo IIA configurations with the T-segment retained in the C-gate, provide data to further understand these terminal steps.

An important observation was a high conformational flexibility of the N-gate, especially in ATP-hydrolyzed (**2Bro**, **3Rel**) or apo (**4Rel**) configurations. RMSD and PCA analyses revealed significant twisting and opening motions of the ATPase domains, with **4Rel** (no bound nucleotides) predominantly retaining an open N-gate conformation. This supports the proposed role of the N-gate as the exit path for the G-segment following ATP hydrolysis and ADP release and suggest that this open state is readily accessible once the ADPs vacate the binding site.

By contrast, the C-gate remained structurally rigid when it housed the T-segment. PCA also revealed only minor local protein essential motions, including subtle sliding at the C-gate interface and a swinging movement of the substructure of the TOPRIM domain that engages the T-segment. MM/GBSA calculations further indicated that the T-segment also stably bound in the C-gate seeming even stronger than in the N-gate during earlier catalytic stages, highlighting the C-gate's role not only as an exit point but also as a transient holding site this topo IIA configuration. These observations align with the recently reported crystal structures showing that the C-gate remains sealed while retaining the T-segment while the open C-gate can only be observed in post-catalytic structures lacking this segment (Fig. S24) [26,46]. C-gate opening was not observed in our simulations, likely due to the limited timescales and/or the substantial energy barrier associated with this conformational change. Biased MD techniques, such as steered molecular dynamics or targeted molecular dynamics, could first be used to generate plausible transition pathways, which would then guide enhanced sampling approaches like metadynamics or umbrella sampling using collective variables such as interdomain distances and hinge angles.

When constructing the topo IIA configurations, residues 1071-1106 and 2268-2303 in chains A and B, which were not resolved in the X-ray structure, were omitted to maintain consistency with our previous simulation setups. The structures of these regions, located at the base of the C-gate, were subsequently examined using AlphaFold 3 [52]. The predicted structure of these segments comprised a flexible structural motif, oriented toward the interior of the C-gate—likely due to the absence of a bound T-segment in the prediction and its inherent flexibility (Fig. S25). Given their position and predicted structural characteristics, it can be certainly presumed these two sections contribute to the stabilization and directional guidance of the T-segment during its retention in the C-gate. While we can only speculate on its exact function at present, the apparent dynamics of this structural element could modulate the residence time of the T-segment in the C-gate through its steric influence alone. In addition, the presence of lysine residues on each of these segments (e.g. Lys1083 on the first monomer) could contribute to proper electrostatic control and positioning of the T-segment, with this effect possibly being modulated by phosphorylation [30]. Future studies, such as point mutations, could further clarify the influence of this segment on the C-gate flexibility and T-segment occupancy.

This contrast in dynamic behavior between the N- and C-gates observed in molecular simulations implies that the two bound DNA segments might dissociate from the enzyme at different kinetic rates. In this context, transient C-gate fluctuations or local destabilization, not captured in the time scales of our unbiased MD simulations, could facilitate the earlier release of the T-segment. Furthermore, additional interdomain coupled dynamics might also be crucial for the coordinated release of both segments.

Importantly, in **1Bro** and **2Bro** conformations the cleaved G-segment is already positioned within a closed DNA-gate, while the T-segment is bound in the C-gate. In such configurations, we cannot investigate the role of mechanical coupling between the DNA-gate and the C-gate dynamics during the transition. Moreover, DCCM analysis revealed increased anticorrelations between the C-gate and residues in the DNA- and N-gates in configurations where the T-segment is bound in the C-gate. This suggests that long-range inter-gate communication likely plays a role in coordinating these transitions. Therefore, simultaneous or mechanically coupled release events, although not directly observed in our simulations, are plausible and could represent a physiologically relevant pathway. Finally, the high flexibility of the N-gate after nucleotide dissociation must also be taken into account. Overall, these results suggest coordinated gate transition events that occur when both segments are released.

Future simulations of topo II configurations that could better investigate G-segment release, DNA-gate closure following T-segment transport, and subsequent T-segment dissociation would be valuable to gain further mechanistic insight. Due to the limited time scales accessible in all-atom simulations, longer coarse-grained simulations could provide additional information. Finally, structural studies in which N-gate reopening is blocked (e.g., with bisdioxopiperazines - ICRF inhibitors that bind at interface between two ATPase protomers) could serve as an experimental strategy to further test how T-segment binding affects C-gate dynamics.

Taken together, our all-atom simulations of several configurations of yeast type IIA topoisomerase offer important mechanistic insights into the final steps following T-segment translocation. ATP and ADP allosterically modulate N-gate dynamics, even in the absence of a T-segment in the N-gate. The T-segment is asymmetrically stabilized in the C-gate by positively charged residues, yet this interaction does not suffice to trigger C-gate opening, which remains conformationally restricted. Instead, T-segment binding allosterically promotes a straighter G-segment DNA conformation, likely facilitating religation and subsequent release. The simulation results suggest coordinated dynamics in the release of the DNA segments, although our current simulations provide only limited insight. Further experimental, computational, and structural studies could provide a deeper understanding of the dynamic

coupling between the DNA- and C-gate residues during T-segment transport, providing a more complete picture of this phase of the catalytic cycle. Our results refine the atomistic understanding of the terminal events in the topo IIA catalytic cycle, highlighting how nucleotide allosteric regulation and distinct dynamics of the N- and C-gates could ensure release of DNA segments and efficient enzyme turnover through allosteric communication across the dimeric topo IIA complex.

4. Computational section

4.1. Construction of topo IIA configurations

The molecular modeling in this paper used our previous work as a foundation; we used the previously derived **"cleaved"** structure and its derivative, the **2Pre** structure. **"Cleaved"** was based on the crystal structure of the fully catalytic topoisomerase IIA homodimer from the yeast *Saccharomyces cerevisiae* (PDB: 4GFH) [19]; in this structure the T-segment is cleaved, and both of its strands are covalently bound to the corresponding catalytic Tyr782 residues [41]. For **2Pre**, a T-segment has been inserted into the N-gate, and the DNA G-segment has been religated [42].

Topo IIA configurations **1Bro** and **2Bro** were obtained from **cleaved** structure by first manually placing the DNA inside the C-gate and then modifying either one or both ATP molecules into ADP by deleting the terminal γ-phosphate to obtain either **1Bro** (ADP/ATP nucleotide pair) or **2Bro** (ADP/ADP nucleotide pair) configurations. The DNA used for T-segment has the same nucleotide sequence as the G-segment present in the crystal structure and was generated in our prior simulations by extracting the DNA and relaxing it separately [41]. In **2Pre** structure, both ATPs were either modified into ADP or were completely removed from the ATP binding sites. The T-segment was removed from the N-gate and manually inserted in the C-gate to an identical position as in **1Bro** and **2Bro** to form **3Rel** and **4Rel** topo IIA configurations with the now vacant N-gate kept in the open position. Supplementary material supplies the 3D coordinates of all topo IIA configurations.

4.2. Molecular dynamics simulations

Generated topo IIA conformations were solvated with TIP3P water molecules [53], with the solute being at least 12 Å away from the edges of the box. To make the systems electroneutral, 93 Na^+ ions were added to **1Bro**, 92 Na^+ ions to **2Bro**, 92 Na^+ ions to **3Rel**, and 86 Na^+ ions to **4Rel** configuration. The final systems used in simulations comprised between 730,000 and 785,000 atoms.

The protein was described with Amber14SB force field [54], while the bsc1 force field was used for the DNA [55]. ATP and ADP parameters were developed by Meagher [56] and Mg^{2+} ions by Åqvist [57]. In topo IIA configurations **1Bro** and **2Bro**, the 5′-end of the nucleic acid is covalently linked to the phosphorylated Tyr782 thus this residue was described with the previously developed and validated parameterized "TYN" residue on the protein and DC4 on the DNA [41].

Classical all-atom molecular dynamics (MD) simulations were carried out with Amber20 software [58]. Geometric optimization was performed beforehand for each configuration by: (1) 10,000 steps of the steepest descent method followed by 20,000 steps of the conjugate gradient method. Next, a canonical (NVT) MD equilibration was performed in four runs of 10,000 steps with a time step of 2 fs and the constraints on all protein atoms gradually released, as the system was progressively heated from 0 to 300 K. The force constants dropped from 100 kcal mol^{-1} $Å^{-2}$ (first run) to 60 kcal mol^{-1} $Å^{-2}$ (second run), and to 30 kcal mol^{-1} $Å^{-2}$ (third run), while the fourth run was unconstrained. In a further step, an isothermal-isobaric (NPT) equilibration run was carried out in two runs with a time step of 2 fs and 100,000 steps in each simulation. In the first run, a force constant of 20 kcal mol^{-1} $Å^{-2}$ was used to constrain the protein, which was removed in the second NPT run. The Berendsen barostat [59] and the Langevin thermostat [60] were used to regulate the systems pressure of 1 bar and the temperature of 300 K, respectively. Periodic boundary conditions were applied [60] and Particle Mesh Ewald (PME) method was used to describe long-range electrostatics [61]. SHAKE algorithm that constrains all bond lengths with hydrogen atoms [62] enabled a time step in the simulation of 2 fs.

The production MD simulations amounted to a total simulation time of 1 microsecond (μs) for each configuration. Two additional replicas with the production run of 500 ns for each topo IIA configuration were also conducted. The independent replica simulation runs were initialized by assigning different initial velocities as well as extending the equilibration phase to yield slightly different starting positions: the preparation/simulation protocol was the same as described above, only the duration of the last NPT equilibration run varied; instead of 100,000 steps, it was set to 110,000 and 120,000. Molecular simulations were performed either on GPU processors of the Ažman Computing Centre at the National Institute of Chemistry in Ljubljana or on the supercomputer HPC Vega at the Institute of Information Science in Maribor.

4.3. Analyses of trajectories

The obtained trajectories were visually inspected and analyzed using *Cpptraj* module of AmberTools22 [63]. Root Mean Square Deviation (RMSD), Root Mean Square Fluctuation (RMSF), and Principal Component Analysis (PCA) were calculated along with distance measurements (e.g. between defined atoms or centers of mass of selected subsections) and hydrogen bond analysis (the cutoff for a hydrogen bond was set to 3.3 Å and 35°). The *MMPBSA.py* program was used to calculate the binding free energy using the Molecular Mechanics/Generalized Born Surface Area (MM/GBSA) method [64]. The Bio3D package [65] (version 2.3–0) in the R environment [66] was used to calculate the Dynamic Cross-Correlation Maps (DCCM). The simulated DNA segments were analyzed using Curves+ [67].

RMSF, distance measurements, H-bond analysis, PCA, DCCM, and DNA parameter calculations, were performed only on the equilibrated part of the trajectories (i.e. 100 to 1000 ns), while the RMSD was calculated over the entire trajectory. The same was applied when analyzing replicas, except that the equilibrated part was between 100 and 500 ns. To compare the results of the initial 1 μs simulation with both replicas, only the first part of the covered simulation (100 to 500 ns) was used. The trajectories were visualized using UCSF Chimera [68], R software [66], PyMOL [69], and Visual Molecular Dynamics (VMD) [70].

4.3.1. Principal component analysis (PCA)

VMD Normal Mode Wizard plugin was used to visualize large-scale collective motions. The R studio software was used to create and diagonalize the covariance matrices of position fluctuations to determine the eigenvalues and the corresponding eigenvectors.

4.3.2. Dynamical cross-correlation map (DCCM) analysis

The Bio3D library [65] in the R environment [66] was used to compute the Dynamic Cross-Correlation Maps (DCCM), which quantify the extent of pairwise residual correlations [71]. The Pearson correlation coefficients (C_{ij}) for the Ca atom paris i and j were calculated using the *dccm* function, which internally derives the covariance matrices:

$$C_{ij} = \frac{c_{ij}}{\left[c_{ij}c_{ij}\right]^{1/2}} = \frac{\left\langle \Delta r_i \bullet \Delta r_j \right\rangle}{\left\langle \Delta r_i^2 \right\rangle^{1/2} \left\langle \Delta r_j^2 \right\rangle^{1/2}}$$

In this equation, c_{ij} is defined as $c_{ij} = \langle \Delta r_i \cdot \Delta r_j \rangle$, where Δr_i is a displacement vector of atom i and Δr_j of atom j, and the angle brackets denote an ensemble average. If the covariances are normalized as described above, the cross-correlation coefficient C_{ij} can be determined. PyMOL software was used to visualize the correlated and anticorrelated movements corresponding to the residues in the matrices [69].

4.3.3. MM/GBSA free energy calculations

The converged part of each trajectory was utilized to obtain 500 input snapshots which were taken at equidistant intervals. *MMPBSA.py* used the Generalized Born IGB method 5 (igb = 5) [72] with the salt concentration to 0.1 M in the calculations of the binding free energy. Per residue decomposition of the binding free energy was also performed. The MM/GBSA calculations were performed between the topo IIA and nucleotides (ATP/ADP), T-segment, and G-segment of the DNA. To investigate the interactions between the homodimers in each of the topo IIA configurations, these calculations were also performed with one of the topo IIA protein monomers as a ligand.

4.3.4. Analysis of DNA structure

The conformations of nucleic acids of the bound G-segment DNA segments were analyzed on the equilibrated part of the trajectories with Curves+ [67]. All snapshots of the part of the trajectory were considered to obtain better sampling. On slide and x-displacement plots (Fig. S22-S23), for clarity reasons the results are averaged from 2250 to 200 data points, while in the Tables S20-S21 all data points were considered.

Supplementary data to this article can be found online at https://doi.org/10.1016/j.ijbiomac.2025.147216.

CRediT authorship contribution statement

Kristina Stevanović: Writing – review & editing, Writing – original draft, Visualization, Investigation, Formal analysis. **Barbara Herlah:** Writing – review & editing, Writing – original draft, Visualization, Investigation, Formal analysis. **Matic Pavlin:** Writing – review & editing, Writing – original draft, Investigation, Formal analysis. **Andrej Perdih:** Writing – review & editing, Writing – original draft, Supervision, Resources, Investigation.

Declaration of competing interest

The authors declare the following financial interests/personal relationships which may be considered as potential competing interests: Given his role as Editor, dr. Andrej Perdih had no involvement in the peer review of this article and had no access to information regarding its peer review. Full responsibility for the editorial process for this article was delegated to another journal editor. If there are other authors, they declare that they have no known competing financial interests or personal relationships that could have appeared to influence the work reported in this paper.

Acknowledgments

This work was supported by the Slovenian Research and Innovation Agency (ARIS) through a research project J1-4402 (A.P. and K.S), young researcher grant (B.H.) and research programs P1-0012 (A.P.) and P2-0421 (M.P.) We kindly acknowledge Ažman high-performance computing (HPC) center at the National Institute of Chemistry in Ljubljana, Slovenia for computational resources. The authors also acknowledge the HPC-RIVR consortium (Project ID S24O01-17) and EuroHPC for funding this research by providing computing resources of the HPC system Vega at the Institute of Information Science. Dr. Matej Janežič is thanked for critical reading of the manuscript and Jan Van Elteren for technical assistance.

Data availability

Molecular dynamics simulations, analysis, and visualizations were performed with programs: Amber20, AmberTools22, VMD 1.9.3, UCSF Chimera, Xmgrace, R software environment with the Bio3D library 2.3-0, PyMol 2.0, and Curves+. The starting structure for simulations was obtained from the Protein Data Bank (PDB) public database. All procedures and workflows are described in the Methods section. Starting structures used for MD simulations are provided in Supplementary material.

References

[1] J.C. Wang, Moving one DNA double helix through another by a type II DNA topoisomerase: the story of a simple molecular machine, Q. Rev. Biophys. 31 (2) (1998) 107–144.
[2] S.M. Vos, E.M. Tretter, B.H. Schmidt, J.M. Berger, All tangled up: how cells direct, manage and exploit topoisomerase function, Nat. Rev. Mol. Cell Biol. 12 (12) (2011) 827–841.
[3] Y. Pommier, Y. Sun, S.N. Huang, J.L. Nitiss, Roles of eukaryotic topoisomerases in transcription, replication and genomic stability, Nat. Rev. Mol. Cell Biol. 17 (11) (2016) 703–721.
[4] J.C. Wang, Interaction between DNA and an Escherichia coli protein omega, J. Mol. Biol. 55 (3) (1971) 523–533.
[5] J.L. Nitiss, Targeting DNA topoisomerase II in cancer chemotherapy, Nat. Rev. Cancer 9 (5) (2009) 338–350.
[6] C. Bailly, Contemporary challenges in the design of topoisomerase II inhibitors for cancer chemotherapy, Chem. Rev. 112 (7) (2012) 3611–3640.
[7] C.A. Felix, Secondary leukemias induced by topoisomerase-targeted drugs, Biochim. Biophys. Acta 1400 (1–3) (1998) 233–255.
[8] B. Pogorelčnik, A. Perdih, T. Solmajer, Recent developments of DNA poisons - human DNA topoisomerase IIα inhibitors - as anticancer agents, Curr. Pharm. Des. 19 (13) (2013) 2474–2488.
[9] B. Pogorelčnik, A. Perdih, T. Solmajer, Recent advances in the development of catalytic inhibitors of human DNA topoisomerase IIα as novel anticancer agents, Curr. Med. Chem. 20 (5) (2013) 694–709.
[10] K. Bergant Loboda, M. Janezič, M. Štampar, B. Žegura, M. Filipič, A. Perdih, Substituted 4,5'-Bithiazoles as catalytic inhibitors of human DNA topoisomerase IIα, J. Chem. Inf. Model. 60 (7) (2020) 3662–3678.
[11] B. Herlah, M. Janežič, I. Ogris, S.G. Grdadolnik, K. Kološa, S. Žabkar, B. Žegura, A. Perdih, Nature-inspired substituted 3-(imidazol-2-yl) morpholines targeting human topoisomerase IIα: Dynophore-derived discovery, Biomed. Pharmacother. 175 (2024) 116676.
[12] B. Herlah, T. Goričan, N.S. Benedik, S.G. Grdadolnik, I. Sosič, A. Perdih, Simulation- and AI-directed optimization of 4,6-substituted 1,3,5-triazin-2(1H)-ones as inhibitors of human DNA topoisomerase IIα, Comput. Struct. Biotechnol. J. 23 (2024) 2995–3018.
[13] V. Vidmar, M. Vayssieres, V. Lamour, What's on the other side of the gate: a structural perspective on DNA gate opening of type IA and IIA DNA topoisomerases, Int. J. Mol. Sci. 24 (4) (2023) 3986.
[14] R.B. Tennyson, J.E. Lindsley, Type II DNA topoisomerase from Saccharomyces cerevisiae is a stable dimer, Biochemistry 36 (20) (1997) 6107–6114.
[15] S.F. Chen, N.L. Huang, J.H. Lin, C.C. Wu, Y.R. Wang, Y.J. Yu, M.K. Gilson, N. L. Chan, Structural insights into the gating of DNA passage by the topoisomerase II DNA-gate, Nat. Commun. 9 (1) (2018) 3085.
[16] K.C. Dong, J.M. Berger, Structural basis for gate-DNA recognition and bending by type IIA topoisomerases, Nature 450 (7173) (2007) 1201–1205.
[17] H. Wei, A.J. Ruthenburg, S.K. Bechis, G.L. Verdine, Nucleotide-dependent domain movement in the ATPase domain of a human type IIA DNA topoisomerase, J. Biol. Chem. 280 (44) (2005) 37041–37047.
[18] E.M. Ling, A. Basle, I.G. Cowell, B. van den Berg, T.R. Blower, C.A. Austin, A comprehensive structural analysis of the ATPase domain of human DNA topoisomerase II beta bound to AMPPNP, ADP, and the bisdioxopiperazine, ICRF193, Structure 30 (8) (2022) 1129–1145, e1123.
[19] B.H. Schmidt, N. Osheroff, J.M. Berger, Structure of a topoisomerase II-DNA-nucleotide complex reveals a new control mechanism for ATPase activity, Nat. Struct. Mol. Biol. 19 (11) (2012) 1147–1154.
[20] R. Dutta, M. Inouye, GHKL, an emergent ATPase/kinase superfamily, Trends Biochem. Sci. 25 (1) (2000) 24–28.
[21] C.C. Chang, Y.R. Wang, S.F. Chen, C.C. Wu, N.L. Chan, New insights into DNA-binding by type IIA topoisomerases, Curr. Opin. Struct. Biol. 23 (1) (2013) 125–133.
[22] B.H. Schmidt, A.B. Burgin, J.E. Deweese, N. Osheroff, J.M. Berger, A novel and unified two-metal mechanism for DNA cleavage by type II and IA topoisomerases, Nature 465 (7298) (2010) 641–644.
[23] K. Shintomi, T. Hirano, Guiding functions of the C-terminal domain of topoisomerase IIα advance mitotic chromosome assembly, Nat. Commun. 12 (1) (2021) 2917.
[24] D.J. Clarke, Y. Azuma, Non-catalytic roles of the topoisomerase IIα C-terminal domain, Int. J. Mol. Sci. 18 (11) (2017) 2438.
[25] A. Vanden Broeck, C. Lotz, R. Drillien, L. Haas, C. Bedez, V. Lamour, Structural basis for allosteric regulation of human topoisomerase IIalpha, Nat. Commun. 12 (1) (2021) 2962.
[26] J. Yang, Z. Shao, X. Zhao, W. Zhang, Y. Zhang, L. Li, Y. Gao, Q. Shao, C. Cao, H. Li, et al., Structures of African swine fever virus topoisomerase complex and their implications, Nat. Commun. 15 (1) (2024) 6484.
[27] J. Cong, Y. Xin, H. Kang, Y. Yang, C. Wang, D. Zhao, X. Li, Z. Rao, Y. Chen, Structural insights into the DNA topoisomerase II of the African swine fever virus, Nat. Commun. 15 (1) (2024) 4607.
[28] C.M. Chang, S.C. Wang, C.H. Wang, A.H. Pang, C.H. Yang, Y.K. Chang, W.J. Wu, M. D. Tsai, A unified view on enzyme catalysis by cryo-EM study of a DNA topoisomerase, Commun. Chem. 7 (1) (2024) 45.

[29] C. Lotz, V. Lamour, The interplay between DNA topoisomerase 2α post-translational modifications and drug resistance, Cancer Drug Resist. 3 (2) (2020) 149–160.
[30] C. Bedez, C. Lotz, C. Batisse, A.V. Broeck, R.H. Stote, E. Howard, K. Pradeau-Aubreton, M. Ruff, V. Lamour, Post-translational modifications in DNA topoisomerase 2α highlight the role of a eukaryote-specific residue in the ATPase domain, Sci. Rep. 8 (1) (2018) 9272.
[31] J. Lee, M. Wu, J.T. Inman, G. Singh, S.H. Park, J.H. Lee, R.M. Fulbright, Y. Hong, J. Jeong, J.M. Berger, et al., Chromatinization modulates topoisomerase II processivity, Nat. Commun. 14 (1) (2023) 6844.
[32] J. Roca, J.C. Wang, DNA transport by a type II DNA topoisomerase: evidence in favor of a two-gate mechanism, Cell 77 (4) (1994) 609–616.
[33] J. Roca, J.C. Wang, The capture of a DNA double Helix by an ATP-dependent protein clamp: a key step in DNA transport by type II DNA topoisomerases, Cell 71 (5) (1992) 833–840.
[34] S. Lee, S.R. Jung, K. Heo, J.A. Byl, J.E. Deweese, N. Osheroff, S. Hohng, DNA cleavage and opening reactions of human topoisomerase IIα are regulated via Mg2 + −mediated dynamic bending of gate-DNA, Proc. Natl. Acad. Sci. USA 109 (8) (2012) 2925–2930.
[35] C.L. Baird, T.T. Harkins, S.K. Morris, J.E. Lindsley, Topoisomerase II drives DNA transport by hydrolyzing one ATP, Proc. Natl. Acad. Sci. USA 96 (24) (1999) 13685–13690.
[36] M. Ogrizek, M. Janežič, K. Valjavec, A. Perdih, Catalytic mechanism of ATP hydrolysis in the ATPase domain of human DNA topoisomerase IIα, J. Chem. Inf. Model. 62 (16) (2022) 3896–3909.
[37] A.D. Bates, A. Maxwell, Energy coupling in type II topoisomerases: why do they hydrolyze ATP? Biochemistry 46 (27) (2007) 7929–7941.
[38] A.D. Bates, J.M. Berger, A. Maxwell, The ancestral role of ATP hydrolysis in type II topoisomerases: prevention of DNA double-strand breaks, Nucleic Acids Res. 39 (15) (2011) 6327–6339.
[39] A.F. Bandak, T.R. Blower, K.C. Nitiss, V. Shah, J.L. Nitiss, J.M. Berger, Using energy to go downhill-a genoprotective role for ATPase activity in DNA topoisomerase II, Nucleic Acids Res. 52 (3) (2024) 1313–1324.
[40] C. Skouboe, L. Bjergbaek, V.H. Oestergaard, M.K. Larsen, B.R. Knudsen, A. H. Andersen, A human topoisomerase IIα heterodimer with only one ATP binding site can go through successive catalytic cycles, J. Biol. Chem. 278 (8) (2003) 5768–5774.
[41] M. Pavlin, B. Herlah, K. Valjavec, A. Perdih, Unveiling the interdomain dynamics of type II DNA topoisomerase through all-atom simulations: implications for understanding its catalytic cycle, Comput. Struct. Biotechnol. J. 21 (2023) 3746–3759.
[42] B. Herlah, M. Pavlin, A. Perdih, Molecular choreography: unveiling the dynamic landscape of type IIA DNA topoisomerases before T-segment passage through all-atom simulations, Int. J. Biol. Macromol. 269 (2024) 131991.
[43] B. Knapp, L. Ospina, C.M. Deane, Avoiding false positive conclusions in molecular simulation: the importance of replicas, J. Chem. Theory Comput. 14 (12) (2018) 6127–6138.
[44] T.T. Harkins, T.J. Lewis, J.E. Lindsley, Pre-steady-state analysis of ATP hydrolysis by Saccharomyces cerevisiae DNA topoisomerase II. 2. Kinetic mechanism for the sequential hydrolysis of two ATP, Biochemistry 37 (20) (1998) 7299–7312.
[45] E.M. Smith, A. Mondragon, Basic residues at the C-gate of DNA gyrase are involved in DNA supercoiling, J. Biol. Chem. 297 (2) (2021) 101000.
[46] T.J. Wendorff, B.H. Schmidt, P. Heslop, C.A. Austin, J.M. Berger, The structure of DNA-bound human topoisomerase IIα: conformational mechanisms for coordinating inter-subunit interactions with DNA cleavage, J. Mol. Biol. 424 (3–4) (2012) 109–124.
[47] I. Daidone, A. Amadei, Essential dynamics: foundation and applications, WIREs Comput. Mol. Sci. 2 (5) (2012) 762–770.
[48] N. Stantial, A. Rogojina, M. Gilbertson, Y. Sun, H. Miles, S. Shaltz, J. Berger, K. C. Nitiss, S. Jinks-Robertson, J.L. Nitiss, Trapped topoisomerase II initiates formation of de novo duplications via the nonhomologous end-joining pathway in yeast, Proc. Natl. Acad. Sci. USA 117 (43) (2020) 26876–26884.
[49] S. Bendsen, V.H. Oestergaard, C. Skouboe, M. Brinch, B.R. Knudsen, A. H. Andersen, The QTK loop is essential for the communication between the N-terminal ATPase domain and the central cleavage-ligation region in human topoisomerase IIα, Biochemistry 48 (27) (2009) 6508–6515.
[50] L. Bjergbaek, P. Kingma, I.S. Nielsen, Y. Wang, O. Westergaard, N. Osheroff, A. H. Andersen, Communication between the ATPase and cleavage/religation domains of human topoisomerase IIα, J. Biol. Chem. 275 (17) (2000) 13041–13048.
[51] W.K. Olson, M. Bansal, S.K. Burley, R.E. Dickerson, M. Gerstein, S.C. Harvey, U. Heinemann, X.J. Lu, S. Neidle, Z. Shakked, et al., A standard reference frame for the description of nucleic acid base-pair geometry, J. Mol. Biol. 313 (1) (2001) 229–237.
[52] J. Abramson, J. Adler, J. Dunger, R. Evans, T. Green, A. Pritzel, O. Ronneberger, L. Willmore, A.J. Ballard, J. Bambrick, et al., Accurate structure prediction of biomolecular interactions with AlphaFold 3, Nature 630 (8016) (2024) 493–500.
[53] W. Jorgensen, J. Chandrasekhar, J. Madura, R. Impey, M. Klein, Comparison of simple potential functions for simulating liquid water, J. Chem. Phys. 79 (1983) 926–935.
[54] J.A. Maier, C. Martinez, K. Kasavajhala, L. Wickstrom, K.E. Hauser, C. Simmerling, ff14SB: improving the accuracy of protein side chain and backbone parameters from ff99SB, J. Chem. Theory Comput. 11 (8) (2015) 3696–3713.
[55] I. Ivani, P.D. Dans, A. Noy, A. Perez, I. Faustino, A. Hospital, J. Walther, P. Andrio, R. Goni, A. Balaceanu, et al., Parmbsc1: a refined force field for DNA simulations, Nat. Methods 13 (1) (2016) 55–58.
[56] K.L. Meagher, L.T. Redman, H.A. Carlson, Development of polyphosphate parameters for use with the AMBER force field, J. Comput. Chem. 24 (9) (2003) 1016–1025.
[57] J. Åqvist, Ion-water interaction potentials derived from free energy perturbation simulations, J. Phys. Chem. 94 (21) (1990) 8021–8024.
[58] D.A. Case, K. Belfon, I.Y. Ben-Shalom, S.R. Brozell, D.S. Cerutti, I.T.E. Cheatham, V. W.D. Cruzeiro, T.A. Darden, R.E. Duke, G. Giambaşu, M.K. Gilson, H. Gohlke, A. W. Goetz, R. Harris, S. Izadi, S.A. Izmailov, K. Kasavajhala, A. Kovalenko, R. Krasny, T. Kurtzman, T.S. Lee, S. LeGrand, P. Li, C. Lin, J. Liu, T. Luchko, R. Luo, V. Man, K.M. Merz, Y. Miao, O. Mikhailovskii, G. Monard, H. Nguyen, A. Onufriev, S.P. Pan, S. Pantano, R. Qi, D.R. Roe, A. Roitberg, C. Sagui, S. Schott-Verdugo, J. Shen, C.L. Simmerling, N.R. Skrynnikov, J. Smith, J. Swails, R.C. Walker, J. Wang, L. Wilson, R.M. Wolf, X. Wu, Y. Xiong, Y. Xue, D.M. York, P.A. Kollman, AMBER 2020, University of California, San Francisco, 2020.
[59] H.J.C. Berendsen, J.P.M. Postma, W.F. van Gunsteren, A. DiNola, J.R. Haak, Molecular dynamics with coupling to an external bath, J. Chem. Phys. 81 (8) (1984) 3684–3690.
[60] G.S. Grest, K. Kremer, Molecular dynamics simulation for polymers in the presence of a heat bath, Phys Rev A Gen Phys 33 (5) (1986) 3628–3631.
[61] T. Darden, D. York, L. Pedersen, Particle mesh Ewald: an N·log(N) method for Ewald sums in large systems, J. Chem. Phys. 98 (12) (1993) 10089–10092.
[62] J.-P. Ryckaert, G. Ciccotti, H.J.C. Berendsen, Numerical integration of the cartesian equations of motion of a system with constraints: molecular dynamics of n-alkanes, J. Comput. Phys. 23 (3) (1977) 327–341.
[63] D.A. Case, H.M. Aktulga, K. Belfon, I.Y. Ben-Shalom, J.T. Berryman, S.R. Brozell, D. S. Cerutti, I.T.E. Cheatham, G.A. Cisneros, V.W.D. Cruzeiro, T.A. Darden, N. Forouzesh, G. Giambaşu, T. Giese, M.K. Gilson, H. Gohlke, A.W. Goetz, J. Harris, S. Izadi, S.A. Izmailov, K. Kasavajhala, M.C. Kaymak, E. King, A. Kovalenko, T. Kurtzman, T.S. Lee, P. Li, C. Lin, J. Liu, T. Luchko, R. Luo, M. Machado, V. Man, M. Manathunga, K.M. Merz, Y. Miao, O. Mikhailovskii, G. Monard, H. Nguyen, K. A. O'Hearn, A. Onufriev, S.P.F. Pan, A.R.R. Qi, D.R. Roe, A. Roitberg, C. Sagui, S. Schott-Verdugo, A. Shajan, J. Shen, C.L. Simmerling, N.R. Skrynnikov, J. Smith, J. Swails, R.C. Walker, J. Wang, J. Wang, H. Wei, X. Wu, Y. Wu, Y. Xiong, Y. Xue, D.M. York, S. Zhao, Q. Zhu, P.A. Kollman, AMBER 2022, University of California, San Francisco, 2022.
[64] I. Massova, P.A. Kollman, Combined molecular mechanical and continuum solvent approach (MM-PBSA/GBSA) to predict ligand binding, Perspect Drug Discov Des 18 (1) (2000) 113–135.
[65] B.J. Grant, A.P. Rodrigues, K.M. ElSawy, J.A. McCammon, L.S. Caves, Bio3d: an R package for the comparative analysis of protein structures, Bioinformatics 22 (21) (2006) 2695–2696.
[66] R: A Language and Environment for Statistical Computing, R Foundation for Statistical Computing, 2018.
[67] C. Blanchet, M. Pasi, K. Zakrzewska, R. Lavery, CURVES+ web server for analyzing and visualizing the helical, backbone and groove parameters of nucleic acid structures, Nucleic Acids Res. 39 (2011) (Web Server issue), W68-73).
[68] E.F. Pettersen, T.D. Goddard, C.C. Huang, G.S. Couch, D.M. Greenblatt, E.C. Meng, T.E. Ferrin, UCSF chimera—a visualization system for exploratory research and analysis, J. Comput. Chem. 25 (13) (2004) 1605–1612.
[69] L. Schrodinger, The PyMOL Molecular Graphics System, 2015.
[70] W. Humphrey, A. Dalke, K. Schulten, VMD: visual molecular dynamics, J. Mol. Graph. Model. 14 (1) (1996) 33–38.
[71] A. Bakan, L.M. Meireles, I. Bahar, ProDy: protein dynamics inferred from theory and experiments, Bioinformatics 27 (11) (2011) 1575–1577.
[72] B.R. Miller 3rd, T.D. McGee Jr., J.M. Swails, N. Homeyer, H. Gohlke, A.E. Roitberg, MMPBSA.Py: an efficient program for end-state free energy calculations, J. Chem. Theory Comput. 8 (9) (2012) 3314–3321.